(Title Page)

Contact Acoustic Nonlinearity Effect on the Vibro-acoustic Modulation of Delaminated Composite Structures

Yi He[1], Yi Xiao[1*], Zhongqing Su[2], Yongdong Pan[1] and Zhen Zhang[1]

(1. School of Aerospace Engineering and Applied Mechanics Tongji University, Shanghai 200092, China)

(2. Department of Mechanical Engineering the Hong Kong Polytechnic University, Hong Kong, China)

Corresponding author: +86 2165983674. Email: y_xiao@tongji.edu.cn

Abstract: In recent years, Vibro-Acoustic Modulation (VAM) techniques for structural health monitoring have received increasing attention. For such techniques, the sidebands and higher-order harmonics generated by double/single sinusoidal excitations are utilized to identify a series of damages. Currently, most VAM investigations are experimental, mainly involving signal processing, while few studies have paid attention to the mechanics of VAM generation. This paper presents a comprehensive investigation which studies the effects of Contact Acoustic Nonlinearity (CAN) on VAM for delaminated composite structures. The paper includes theoretical analysis, simulations, and experiments. Considering both a nonlinear contact constitutive model and the clapping/rubbing discontinuity, an approximate solution for nonlinear motional equation was established by using Fourier series expansion. A modified Greenwood-Williamson (GW) model for physical contact was implemented into the commercial finite element software ABAQUS by a UINTER subroutine, which described the contact behaviors between rough surfaces. The calculated signal responses from the delaminated composite plates were compared to experimental results. A good agreement was qualitatively and quantitatively achieved with acceptable error. Particularly, some specific features of higher-order sidebands existing in the experiment were identified. Results showed that the combined effect of the nonlinear contact constitutive model and the clapping/rubbing mechanism caused odd-even order differences. The asymmetry between the sidebands indicates the existence of amplitude and frequency modulations, which can be used to extract nonlinear damage indexes. These indexes are capable of characterizing the degree and range of damage.

Keywords: composite structures; structural health monitoring; vibro-acoustic modulation; contact acoustic nonlinearity; amplitude modulation; frequency modulation

(Text)

1 Introduction

Composite structures, under complex loading conditions and impact from unexpected catastrophic accidents, are prone to delamination. To avoid catastrophic incidents, structural health monitoring (SHM) methods for composite structures have been developed. In the early stages, conventional linear-feature-based SHM approaches which employed modal analysis, Lamb wave and acoustic emission testing were widely used to detect delamination in composite structures [1,2]. However, due to their weak sensitivity and inability to detect initial damage, the utilization of linear-feature-based SHM methods is greatly limited. Therefore, novel nonlinear-feature-based SHM methods, and especially Vibro-Acoustic Modulation (VAM) technique, gained increasing attention subsequently.

In general, modulation is generated when a nonlinear system (mixer) is excited by two single-frequency sinusoidal signals. In this study, the “nonlinear system” represents a damaged structure, and the signals are called pump and probe waves for lower-frequency (LF) and higher-frequency (HF) excitations, respectively. In mechanical systems, there are generally two types of acoustic nonlinearity: motional and medium nonlinearity. Motional nonlinearity exists in hydrodynamics when the Mach number equals 1, but does not exist in solid mediums [3]. Medium nonlinearity can be divided into two classifications: material nonlinearity and contact acoustic nonlinearity (CAN) [4]. Material nonlinearity is present in materials that possesses nonlinear stress-strain behavior, such as plasticity and hyperelasticity, etc. On the other hand, CAN is present at interfacial contact, such as, delamination and bolted joints [5]. CAN is considered to be the major factor causing nonlinearity in damaged structures [6].

Initially, based on their previous study on liquids, Breazeale et al. [7,8] proposed that a waveform would be distorted when a high-intensity ultrasonic wave passed through a nonlinear or anharmonic solid. This indicates the generation of higher-order harmonics of the fundamental frequency, laying the foundation for nonlinear-feature-based SHM methods. When they are loaded, materials obeying Hooke’s law may also develop local anharmonicity. Akira et al. [9] investigated acoustic waves propagating in metals with local dislocation displacements and found a second-order harmonic. In addition, the amplitude of the second-order harmonic was found to change as a linear function of the fundamental wave amplitude and increased with increasing tensile bias stress. The harmonic would also increase when an ultrasonic wave passed through unbonded interfaces of a linear material [10,11]. Subsequently, Buck et al. [10,12] used ultrasonic harmonic generation to successfully establish a nondestructive testing (NDT) technique for detecting fatigue cracks in aluminum. They also proposed a near-linear relationship between second-order harmonic amplitude and fatigue crack size.

Most recent research on harmonics have been focusing on the nonlinear Lamb wave. For instance, Shkerdin et al. [13,14] investigated the nonlinear interaction between Lamb wave and bilayer containing delamination by a quasi-stationary approach. The localization result showed that harmonics provided a higher delamination detection contrast and spatial resolution with respect to the linear acoustics. Soleimanpour et al. [15,16] conducted explicit simulation and transducer network experiment for locating delamination, which displayed the delamination clapping effect generated bidirectional higher harmonics. Yelve et al. [17] provided a spectral damage index (SDI), which joins peaks of the first three harmonics by a series of lines to obtain the tangent of the spectral envelop angle θ. SDI is invariant to the sensor location and decreases with delamination width. This represents a potential in characterizing the degree of damage.

Donskoy and Sutin [18,19] exploited the VAM technique to identify structural damages. In their studies, the stiffness was phenomenologically abstracted as a quadratic or cubic multivariate function, a Taylor-series simplification. The coefficient of the quadratic or cubic item was a nonlinear coefficient that was determined experimentally. For the quantitative characterization of damage, several damage indexes (DIs) have been defined. Duffour et al. [20] proposed the ratio of the first sideband amplitude to the carrier amplitude as a definition for the DI. Despite being able to identify the existence of cracks, the DI does not have a positive correlation with crack size.

In recent years, VAM has been introduced into composite SHM. Solodov et al. [21] experimentally investigated the self-modulation of composite structures and found a high locality of nonlinear response, which indicated VAM's potential to detect and locate delamination. Meo et al. [22] discovered higher nonlinear signals in sandwich structures compared to metals, where more than fourth-order harmonics and sidebands were obtained. Aymerich and Staszewski [23,24] clarified the piecewise nonlinearity of CAN, demonstrating that there are at least two different CANs, namely, nonlinear contact pressure-displacement relationship and clapping. The selection of excitation frequency was discussed, and their results demonstrated that selecting the optimal modal frequency for excitation could increase the VAM response. This indicates that the modal frequency could excite stronger contact motion. Some tests performed on composite structures exhibited special VAM and harmonic phenomena, consisting of asymmetrical sidebands and odd-even differences that could not be explained by the Taylor-series-based method [25]. Chen et al. [26] compared a VAM DI with a harmonic DI and showed that the former had better sensitivity. In a series of studies, Klepka et al. [27-30] explored the effect of different crack modes, using the finite element method (FEM) and relevant signal processing methods, on the VAM for multiple composite structures. A piecewise linear continuous function around the delamination was established and approximated by a polynomial, while the delamination was simulated by a doubled-node approach. Ooijevaar et al. [31] decomposed the original experimental VAM signal and found that there were two components, namely amplitude modulation (AM) and frequency modulation (FM). In addition, the spatial results illustrated that the nonlinear signal possessed great locality, useful for identifying the location of defects. Ashish et al. [32,33] proposed a generic 3D theory to explain VAM generation and developed a finite element model in the FEM simulation software ABAQUS based on the hard contact constraint, where the damage mapping method using sideband indices evidently displayed the approximate shape and position of the delamination. Furthermore, a sweep was used as the pump wave, and results showed that it could significantly decrease the frequency-dependence compared to a sine pump wave [34,35].

Despite long-term investigations on contact linearity in statics, studies focusing on the physical background of CANs are limited [36-39]. Most contact models were based on the Hertz contact model that describes the behavior when two micro-hemispherical elastomers contact with each other. Subsequently, Greenwood and Williamson [36] established a model to extend the Hertz model, known as the GW model, describing the mechanical behavior of two rough plates that are in contact. Several modifications have been proposed to extend the applicability of the GW model. For example, a Gaussian distribution was employed to describe the normal height statistics of micro-peaks in the original GW model. Afterwards, Adler et al. [37] and Brown et al. [38] corrected the Gaussian distribution to a chi-square distribution and the modified contact pressure-displacement curve corresponded better with the experimental. Baltazar et al. [39] discussed the effect of the dislocation angle, and provided two correction factors: normal and tangential. By taking the dislocation angle into account, the error between the predicted curve and the experimental one further shrunk.

Based on the above literature review, little attention has been paid to exploring how the CAN induces the generation of modulation. Especially, there is a lack of a physical illustration for the mechanism of CAN on the delamination of composite material. In addition, relevant FEMs seem to be outdated for modeling the specific nonlinear contact stiffness, which is usually equivalent to a quadratic function, phenomenologically. The nonlinear contact behavior should be controlled more precisely. To tackle these issues, this paper presents a comprehensive VAM investigation based on both the modified GW model and the clapping/rubbing discontinuity. Firstly, a Fourier-series-expansion-based approximation theory is established to satisfy the first-order discontinuity caused by the clapping/rubbing mechanism. Secondly, a modified GW model is introduced into FEM by a user-defined interaction (UINTER) subroutine [40] that is a subroutine provided by ABAQUS and allows to code the user-defined model to control the interaction between contact faces. Subsequently, a series of delaminated composite plate FEM models are calculated and verified experimentally. Finally, several nonlinear DIs are extracted from original modulation signals to identify the degree and range of delamination.

2 Physical CAN-based vibro-acoustic modulation theory

In this paper, the derivation is based on three basic hypotheses: firstly, the structure does not display material nonlinearity; secondly, the nonlinearity is generated by damage only, i.e., nonlinear contact stiffness K_c; and thirdly, the damping is omitted. For the discussed composite material, the first two hypotheses are reasonable as all the material nonlinearities, consisting of the plasticity, the hyperelasticity, or any other nonlinear elasticity, do not manifest when the composite material only withstands micro-amplitude deformation aroused by ultrasound transmitted to the structure. For the third hypothesis, the energy dissipation is not concerned in this paper, since the steady-state vibration is studied here, which is also consistent with previous investigations [5,31,32]. As a result of the no damping hypothesis, the displacement field can be assumed to have a consistent phase. Fig. 1 shows a typical delaminated composite plate with an in-plane delamination present in the interior of the plate. When the delaminated composite plate is loaded, the upper and lower rough delaminated interfaces perform an opening-closing motion which caused local contact. The strength of contact may strongly depend on the modal shapes, and it will be much stronger when the *z*-direction displacement component in the selected mode plays the main role [31], hence the selection of excitation frequencies should take this into account. A detailed frequency selection will be discussed in the experiment, and the major displacement component used in this section is assumed as *z*-direction, corresponding to contact direction. At the location of contact, a weak VAM wave is generated. The following theoretical analysis determines the evolution of the displacement field at the location of contact.

For simplification, it is assumed that the vibration in the structure has reached a steady-state, and any transient response is neglected. According to the perturbation theory, the displacement field , u, v and w corresponding to *x*, *y* and *z* direction respectively, around the location where contact occurs can be determined by decoupling the displacements as products of modal functions and periodic functions, by the following expression:

$$\begin{aligned} u &= \phi_x(x,y,z)q(t) + \phi_{x0}(x,y,z)q_0(t) \\ v &= \phi_y(x,y,z)q(t) + \phi_{y0}(x,y,z)q_0(t) \\ w &= \phi_z(x,y,z)q(t) + \phi_{z0}(x,y,z)q_0(t) \end{aligned} \tag{1}$$

where ϕ_i and $\phi_{i0}, (i = x, y, z)$, q and q_0 represent modal functions and periodic functions, respectively, and the displacement field is divided into two parts: $\phi_i(x,y,z)q(t)$ represents the linear displacement, and $\phi_{i0}(x,y,z)q_0(t)$ represents the perturbation. Under forced vibration, the equilibrium differential equation can be expressed as:

$$\begin{aligned} &\left(\frac{\partial\sigma_{xx}}{\partial x} + \frac{\partial\tau_{yx}}{\partial y} + \frac{\partial\tau_{zx}}{\partial z}\right) + \left(\frac{\partial\bar{f}_{xx}}{\partial x} + \frac{\partial\bar{f}_{yx}}{\partial y} + \frac{\partial\bar{f}_{zx}}{\partial z}\right) = \rho\frac{\partial^2 u}{\partial t^2} \\ &\left(\frac{\partial\tau_{xy}}{\partial x} + \frac{\partial\sigma_{yy}}{\partial y} + \frac{\partial\tau_{zy}}{\partial z}\right) + \left(\frac{\partial\bar{f}_{xy}}{\partial x} + \frac{\partial\bar{f}_{yy}}{\partial y} + \frac{\partial\bar{f}_{zy}}{\partial z}\right) = \rho\frac{\partial^2 v}{\partial t^2} \\ &\left(\frac{\partial\tau_{xz}}{\partial x} + \frac{\partial\tau_{yz}}{\partial y} + \frac{\partial\sigma_{zz}}{\partial z}\right) + \left(\frac{\partial\bar{f}_{xz}}{\partial x} + \frac{\partial\bar{f}_{yz}}{\partial y} + \frac{\partial\bar{f}_{zz}}{\partial z}\right) = \rho\frac{\partial^2 w}{\partial t^2} \end{aligned} \tag{2}$$

where $\overline{f}_{ij}\left(i, j = x, y, z\right)$ represent the excitation force components, and $\sigma_{ij}\left(i, j = x, y, z\right)$ are the stress components. Being in line with reality, the stiffness along the z-direction is assumed to change due to delamination. Substituting Eq. (1) into Eq. (2), the following motion function is obtained:

$$\begin{aligned} &M_x\ddot{q}\left(t\right)+M_{x0}\ddot{q}_0\left(t\right)+K_x q\left(t\right)+K_{x0}q_0\left(t\right)=\overline{F}_x \\ &M_y\ddot{q}\left(t\right)+M_{y0}\ddot{q}_0\left(t\right)+K_y q\left(t\right)+K_{y0}q_0\left(t\right)=\overline{F}_y \\ &M_z\ddot{q}\left(t\right)+M_{z0}\ddot{q}_0\left(t\right)+K_z q\left(t\right)+K_{z0}q_0\left(t\right)=\overline{F}_z \\ &\boldsymbol{M}\ddot{\boldsymbol{q}}\left(t\right)+\boldsymbol{M}_0\ddot{\boldsymbol{q}}_0\left(t\right)+\boldsymbol{K}\boldsymbol{q}\left(t\right)+\boldsymbol{K}_0\boldsymbol{q}_0\left(t\right)=\boldsymbol{F} \end{aligned} \tag{3}$$

where, the original mass matrix is split into two mass sub-matrices $\boldsymbol{M}$ and $\boldsymbol{M}_0$ due to the existence of perturbation, containing only three diagonal non-zero elements M_i and $M_{i0}\left(i=x,y,z\right)$. Due to combined effect of K_c and perturbation $\boldsymbol{q}_0$, $\boldsymbol{K}$ and $\boldsymbol{K}_0$ exist, representing the two stiffness sub-matrices with only diagonal non-zero elements K_i and $K_{i0}\left(i=x,y,z\right)$. $\boldsymbol{F}$ is the excitation vector with three elements $\overline{F}_i\left(i=x,y,z\right)$. $\boldsymbol{q}$ and $\boldsymbol{q}_0$ are two vectors with all three elements that are equal to q and q_0, respectively. Eq. (3) represents the differential dynamic function of a system with nonlinear displacement components, of which the terms have undergone significant simplification. Their full forms are detailly listed in Appendix I. From Appendix I, it can be noticed that $\boldsymbol{K}$ and $\boldsymbol{K}_0$ are two time-dependent stiffness matrices, since both of them are functions of K_c, which is time-dependent and will be discussed in detail later. However, $\boldsymbol{M}$ and $\boldsymbol{M}_0$ remain time-independent and constant. Thus, Eq. (3) is a non-homogeneous linear differential equation with variable coefficients, or a nonlinear state-variable function. Based on the state-variable method, there are few coefficient forms that can obtain an analytical solution of nonlinear state-variable functions. An analytical solution of Eq. (3) can rarely be obtained in this case, since the modified GW function selected to describe K_c has an open-integration form. However, if only the frequency components are of interest, where this study focuses on, some transformations may be helpful. $\boldsymbol{K}$ and $\boldsymbol{K}_0$ can be further decomposed into the following two sub-matrices, respectively:

$$
\begin{aligned}
&\boldsymbol{K} = \boldsymbol{K}_L + \boldsymbol{K}_N \\
&\quad = diag\left(K_x, K_y, -\left(\left\{\overline{\boldsymbol{C}}\right\}_5 \frac{\partial \boldsymbol{\Phi}}{\partial x} + \left\{\overline{\boldsymbol{C}}\right\}_6 \frac{\partial \boldsymbol{\Phi}}{\partial y} + \left\{\overline{\boldsymbol{C}}\right\}_3 \frac{\partial \boldsymbol{\Phi}}{\partial z} \right) \right) \\
&\quad + diag\left(0, 0, -\left(K_c - \overline{\boldsymbol{C}}_{33} \right) \frac{\partial \boldsymbol{\Phi}}{\partial z} \right) \\
&\boldsymbol{K}_0 = \boldsymbol{K}_{L0} + \boldsymbol{K}_{N0} \\
&\quad = diag\left(K_{x0}, K_{y0}, -\left(\left\{\overline{\boldsymbol{C}}\right\}_5 \frac{\partial \boldsymbol{\Phi}_0}{\partial x} + \left\{\overline{\boldsymbol{C}}\right\}_6 \frac{\partial \boldsymbol{\Phi}_0}{\partial y} + \left\{\overline{\boldsymbol{C}}\right\}_3 \frac{\partial \boldsymbol{\Phi}_0}{\partial z} \right) \right) \\
&\quad + diag\left(0, 0, -\left(K_c - \overline{\boldsymbol{C}}_{33} \right) \frac{\partial \boldsymbol{\Phi}_0}{\partial z} \right)
\end{aligned}
\tag{4}
$$

where, the operator $\{\ \}$ indicates the row vector. $\left\{\overline{\boldsymbol{C}}\right\}_i \left(i = 1, \cdots, 6\right)$ represents the *i*-th row vector of transformed stiffness matrix of composite material $\overline{\boldsymbol{C}}$. Then, Eq. (3) can be transformed into:

$$\boldsymbol{M}\ddot{\boldsymbol{q}}(t) + \boldsymbol{M}_0\ddot{\boldsymbol{q}}_0(t) + \boldsymbol{K}_L\boldsymbol{q}(t) + \boldsymbol{K}_N\boldsymbol{q}(t) + \boldsymbol{K}_{L0}\boldsymbol{q}_0(t) + \boldsymbol{K}_{N0}\boldsymbol{q}_0(t) = \boldsymbol{F} \tag{5}$$

where $\boldsymbol{K}_{N0}\boldsymbol{q}_0$ can be omitted since $\boldsymbol{K}_{N0}$ is derived by using the partial differential perturbation modal function vector $\boldsymbol{\Phi}_0$ and the nonlinear contact stiffness K_c, as presented at Eq.(4), and $\boldsymbol{q}_0$ are the perturbation periodic function, hence the product of them is higher-order infinitesimal. Meanwhile, $-\boldsymbol{K}_N\boldsymbol{q}$ and $\boldsymbol{K}_{L0}\boldsymbol{q}_0$ cannot be omitted, because $\boldsymbol{q}$ is linear periodic function and $\boldsymbol{K}_{L0}$ does not contain K_c. Therefore, Eq. (5) can be rearranged as:

$$\boldsymbol{M}\ddot{\boldsymbol{q}}(t) + \boldsymbol{K}_L\boldsymbol{q}(t) = \boldsymbol{F} \tag{6}$$

$$\boldsymbol{M}_0\ddot{\boldsymbol{q}}_0(t) + \boldsymbol{K}_{L0}\boldsymbol{q}_0(t) = -\boldsymbol{K}_N\boldsymbol{q}(t) \tag{6b}$$

Eq. (6a) is a linear dynamic function, where the frequency components of $\boldsymbol{q}$ are equal to those of $\boldsymbol{F}$, i.e. two fundamental circular frequencies ω_1 and ω_2. As mentioned above, $\boldsymbol{K}$ is time-dependent, however in Eq. (6b), it can be noticed that $\boldsymbol{K}_{L0}$ is a constant matrix, thanks to the decomposition of $\boldsymbol{K}$; thus, Eq. (6b) is a derived constant coefficient dynamic function. Similar to Eq. (6a), the frequency components of $\boldsymbol{q}_0$ are equal to those of virtual excitation $-\boldsymbol{K}_N\boldsymbol{q}(t)$. The following derivation analyzes the frequency components of $-\boldsymbol{K}_N\boldsymbol{q}(t)$. Here, the column vector $\boldsymbol{q}$ is assumed as containing two sinusoidal signals:

$$\boldsymbol{q}=\begin{bmatrix}\sin(\omega_1 t+\theta_1)+\sin(\omega_2 t+\theta_2)\\ \sin(\omega_1 t+\theta_1)+\sin(\omega_2 t+\theta_2)\\ \sin(\omega_1 t+\theta_1)+\sin(\omega_2 t+\theta_2)\end{bmatrix} \tag{7}$$

where, the operator $[\;]$ indicates the column vector. By substitute Eq.(7) into Eq. (4), the $-\boldsymbol{K}_N\boldsymbol{q}(t)$ is obtained:

$$-\boldsymbol{K}_N\boldsymbol{q}(t)=\begin{bmatrix}0\\ 0\\ \dfrac{\partial^2\phi_z}{\partial z^2}\left(K_c-\bar{C}_{33}\right)\left(\sin(\omega_1 t+\theta_1)+\sin(\omega_2 t+\theta_2)\right)\end{bmatrix} \tag{8}$$

The first and second elements of $-\boldsymbol{K}_N\boldsymbol{q}(t)$ are 0, which means that the motion along the *x* and *y* directions is a “free vibration”. Despite that, the damping effect has been omitted for simplification in this paper, in reality it is known that the perturbation in *x* and *y* directions would be damped and attenuated. The K_c is a function of the relative displacement in the contact $\delta(t)$. When the system stays in steady-state vibration, the $\delta(t)$ is a periodic function. Hence, $K_c(\delta(t))$ is also a periodic function with the same circular frequency. This frequency ω is the greatest common divisor of ω_1 and ω_2, satisfying:

$$\omega=\frac{\omega_1}{j}=\frac{\omega_2}{k},\ (j,k\in \mathrm{N}+) \tag{9}$$

Subsequently, by using Fourier series expansion, $K_c(\delta(t))$ can be expressed as follows:

$$\begin{aligned}K_c(\delta(t))&=\frac{k_{a,0}}{2}+\left(\sum_{n=1}^{\infty}\left(k_{a,n}\cos(n\omega t)+k_{b,n}\sin(n\omega t)\right)\right)\\ k_{a,n}&=\frac{\omega}{\pi}\int_{-\pi/\omega_z}^{\pi/\omega_z}K_c(\delta(t))\cos(n\omega t)\,\mathrm{d}t,\ (n=0,1,2,\cdots)\\ k_{b,n}&=\frac{\omega}{\pi}\int_{-\pi/\omega_z}^{\pi/\omega_z}K_c(\delta(t))\sin(n\omega t)\,\mathrm{d}t,\ (n=1,2,3,\cdots)\end{aligned} \tag{10}$$

By substituting Eq.(10) into Eq.(8), the third element of Eq.(8) can be obtained, of which a detailed derivation is attached in Appendix II:

$$\frac{\partial^2 \phi_z}{\partial z^2}\left(\begin{array}{l}\underbrace{\left(\frac{k_{a,0}}{2}-\bar{C}_{33}\right)\left(\sin\left(\omega_1 t+\theta_1\right)+\sin\left(\omega_2 t+\theta_2\right)\right)+}_{\mathrm{I}} \\ \qquad\qquad \underbrace{\frac{1}{2}\sum_{n=1}^{\infty}\sqrt{k_{a,n}^2+k_{b,n}^2}\left(\begin{array}{l}\sin\left(\left(\omega_1+n\omega\right)t+\theta_1-\theta_n\right)+ \\ \sin\left(\left(\omega_1-n\omega\right)t+\theta_1+\theta_n\right)+ \\ \sin\left(\left(\omega_2+n\omega\right)t+\theta_2-\theta_n\right)+ \\ \sin\left(\left(\omega_2-n\omega\right)t+\theta_2+\theta_n\right)\end{array}\right)}_{\mathrm{II}}\end{array}\right) \tag{11}$$

where $\tan\theta_n = k_{b,n}/k_{a,n}$, $\theta_n\left(n\in \mathrm{N}+\right)$ indicates the nonlinearity-induced phase. From Eq.(11) and Eq.(9), the frequency components corresponding to part I and II are presented as:

$$\begin{array}{l}\mathrm{I}\ \left\{ 1)\text{: fundamental frequencies}: \omega_1, \omega_2; \right. \\ \mathrm{II}\left\{\begin{array}{l} 2)\text{: } m\text{-order harmonic of } \omega_1 \text{ and sidebands of } \omega_2\text{: } n\omega = m\omega_1\text{:}\left(m\pm 1\right)\omega_1, \omega_2 \pm m\omega_1; \\ 3)\text{: } m\text{-order harmonic of } \omega_2 \text{ and sidebands of } \omega_1\text{: } n\omega = m\omega_2\text{:}\left(m\pm 1\right)\omega_2, \omega_1 \pm m\omega_2; \\ 4)\text{: frequency division: } \dfrac{n\omega_1}{j} \text{ or } \dfrac{n\omega_2}{k}; \end{array}\right. \\ \left(n, m\in \mathrm{N}+\right)\end{array} \tag{12}$$

According to Eq. (12), a total of 4 frequency components exist: 1) fundamental frequencies ω_1 and ω_2; 2) harmonics of the two fundamental frequencies $i\omega_1$ and $i\omega_2$ $\left(i=2,3,\cdots\right)$; 3) VAM sidebands $\omega_2 \pm i\omega_1$ and $\omega_1 \pm i\omega_2$ $\left(i=1,2,\cdots\right)$; 4) the rest of the components related to the frequency division. With regard to the frequency division, ω_1 and ω_2 are coprime in most selections of excitation frequency, which causes the frequency division energy to spread across the spectrum. Therefore, it is not as significant as the other three components. Based on the above analysis, the frequency components of perturbation $\boldsymbol{q}_0$ are known, which are the same as the ones of the virtual excitation Eq.(8) as shown in Eq.(12).

The amplitude of the VAM sidebands should be further discussed. Taking the first-order sidebands as an example and assuming that $\omega_1 < \omega_2$, the amplitude of $\omega_2+\omega_1$ and $\omega_2-\omega_1$ sidebands are shown as the following, referring to detail derivation in Appendix III:

$$
\begin{aligned}
A_{\omega_1+\omega_2} &= \frac{1}{2}\left(\frac{\partial^2\phi_z}{\partial z^2}\right)\sqrt{k_{a,j}^2+k_{b,j}^2+k_{a,k}^2+k_{b,k}^2+2\sqrt{\left(k_{a,j}^2+k_{b,j}^2\right)\left(k_{a,k}^2+k_{b,k}^2\right)}\cos\left(\theta_2-\theta_j-\theta_1+\theta_k\right)} \\
A_{\omega_1-\omega_2} &= \frac{1}{2}\left(\frac{\partial^2\phi_z}{\partial z^2}\right)\sqrt{k_{a,j}^2+k_{b,j}^2+k_{a,k}^2+k_{b,k}^2-2\sqrt{\left(k_{a,j}^2+k_{b,j}^2\right)\left(k_{a,k}^2+k_{b,k}^2\right)}\cos\left(\theta_2+\theta_j+\theta_1+\theta_k\right)}
\end{aligned} \tag{13}
$$

where， j and k are the constants given by Eq.(9). Due to the phase difference, the right sideband amplitude may not be equal to the left one. It can be further noticed that although the excitation phase difference can be eliminated by setting $\theta_1=\theta_2=0$, the phase difference of the damaged structure still exists, i.e. difference between θ_j and θ_k, which is generated by nonlinearity. This phenomenon indicates that AM and FM may exist simultaneously.

The above derivation has proved the existence of sidebands and harmonics when the structure containing nonlinear contact stiffness K_c. This result satisfies the arbitrary nonlinear form of K_c. The following derivation presents the specific K_c evaluated by using the modified GW model. According to the Hertz model (Fig. 2), every contact hemisphere peak pair can be simplified as a hemispherical elastomer in contact with a rigid plane, which can be described by the following relationship [36,39]:

$$
F_c = \frac{4E^*}{3}R^{*0.5}\delta^{1.5} \tag{14}
$$

Where F_c is contact force, E^* and R^* are the equivalent elastic modulus and the radius of the equivalent hemisphere, respectively, satisfying:

$$
\frac{1}{E^*}=\frac{1-v_1^2}{E_1}+\frac{1-v_2^2}{E_2},\ \frac{1}{R^*}=\frac{1}{R_1}+\frac{1}{R_2} \tag{15}
$$

Where E_i, v_i and $R_i\left(i=1,2\right)$ are the elastic moduli, Poisson ratios and radii of two hemispheres respectively. As an extension of the Hertz model, the modified GW model constitutes a statistical method to equate the contact between two rough surfaces and the contact between a rough surface and a rigid plane (Fig. 3). Then the weighted F_c of every hemisphere peak pair is summed to form normal contact pressure P_c, normal stiffness $K_{c,N}$, contact shear τ_c and tangential stiffness $K_{c,T}$. Ref. [39] provides the detailed derivation:

$$\begin{cases} P_c = \frac{4}{3}\psi_N E^* \beta^{0.5}\eta \int_0^\delta (\delta - z)^{3/2} \varphi(z)\mathrm{dz}, (\delta \ge 0); P_c = 0, (\delta < 0); \\ K_{c,N} = 2\psi_N E^* \beta^{0.5}\eta \int_0^\delta (\delta - z)^{1/2} \varphi(z)\mathrm{dz}, (\delta \ge 0); K_{c,N} = 0, (\delta < 0); \\ \tau_c = \left(8\psi_T G^* \beta^{0.5}\eta \int_0^\delta (\delta - z)^{1/2} \varphi(z)\mathrm{dz} \right)\mathrm{s}, (\delta \ge 0); \tau_c = 0, (\delta < 0); \\ K_{c,T} = 8\psi_T G^* \beta^{0.5}\eta \int_0^\delta (\delta - z)^{1/2} \varphi(z)\mathrm{dz}, (\delta \ge 0); K_{c,T} = 0, (\delta < 0); \end{cases} \tag{16}$$

where β and η represents the average radius and number of the contact hemisphere per unit area. G^* and φ are the equivalent shear module and height distribution of the peaks:

$$\frac{1}{G^*} = \frac{2 - v_1}{G_1} + \frac{2 - v_2}{G_2} \tag{17}$$

$$\varphi(z) = \left(\frac{r_{RMS}}{\sqrt{2n_{chi}}} 2^{n_{chi}} \right)^{-0.5} \frac{z^{0.5(n_{chi}-2)}}{\Gamma(0.5n_{chi})} e^{\left(-\frac{z\sqrt{2n_{chi}}}{2r_{RMS}} \right)} \tag{18}$$

Where Γ is gamma function, and n_{chi} is the degree-of-freedom (DoF) of chi-squared distribution. r_{RMS} refers to the root mean square roughness. In Eq. (16), the clapping and rubbing effects are introduced when the interfaces is detached, i.e. $\delta = 0$. ψ_N and ψ_T represent the average normal and tangential dislocation factors of contact hemisphere peak pairs, respectively, related to the normal and tangential dislocation angles γ and α (Fig. 4):

$$\begin{cases} \psi_N = \cos^{2.5}\gamma + \frac{6G^*}{E^*}\cos^{0.5}\gamma \sin^2\gamma; \\ \psi_T = \frac{1}{\pi}\int_0^{\pi/2} p(\gamma)\mathrm{d}\gamma \int_{-\pi/2}^{\pi/2} 1 - \sin^2\gamma\cos^2\alpha \mathrm{d}\alpha; \end{cases} \tag{19}$$

All the parameters of the modified GW model could be obtained by optical microscopic observation (Wanheng® MM-158C) of the rough surfaces (Fig. 5). The interface edge profiles are outlined, and the height of the peaks were measured to obtain the RMS roughness and fit the Chi-squared probability density function. The rest of the parameters relied on the geometry and the material properties of the contact material, which, in this case, was the fiber of the composite material. All the measured parameters of the modified GW model are listed in Table 1.

3 Finite element implementation

3.1 FEM model of delaminated composite plate

The FEM software ABAQUS has been employed to calculate the nonlinear dynamic response of delaminated composite plates. The hardware platform is a Window 10® workstation including 2 Intel® Xeon® Gold 6128 @3.4GHz CPUs, 64G memory, and a NVIDIA Quadro® P5000 16GB GPU. The time costs for computing 0.1s dynamic responses of the FE-models with 12.5mm 25mm and 50mm delamination cases, corresponding to 10248, 12012 and 15882 elements, are ~24h, ~50h and ~72h in this platform, respectively. A FEM model was set up to simulate the VAM of 6 laminated composite plates with different delamination sizes and locations along the thickness direction. The key points are shown in Fig. 6. The delaminated composite plate was divided into 6 parts, and a user-defined contact pair in the delamination region was defined to control the interaction. The rest of internal surfaces were constrained by *Tie* constraints that provide the continuous deformation condition. Finally, the clamped cantilever boundary condition was applied to the assembly. The LF and HF excitations were applied at two nodes corresponding to their experimental locations. The excitation forms of LF and HF is the sinusoidal displacement and force, respectively. For the trade-off between the computational efficiency and the contact stress accuracy, the element size in the intact area was set as 2.5mm×2.5mm×0.525mm continuum 3-dimensional 8 nodes solid element with reduced integration (C3D8R), whose hourglass effect is slight enough because of the micron-level displacement in this simulation, where the default hourglass control provided by ABAQUS can well settle the minor weakened stiffness brought by reduced integration. Two layers of 1mm × 1mm × 0.525mm continuum 3-dimensional 8 nodes solid element with incompatible modes (C3D8I), which is claimed to provide better accuracy of contact stress results, were laid in the delaminated area [40], as the green elements shown in the lower right subfigure of Fig. 6. To match the actual thickness and layers of the specimen, 4 layers of elements in the thickness direction were set, and 4 composite layers were set in each layer of the element via *Composite Layup Management*, i.e., each layer represents the $[0^\circ/90^\circ_2/0^\circ]$ layup. Specifically, 4 plies were established via *Composite Layup Management*, where the 0° and 90° rotation angles and the material parameters were assigned to the corresponding regions. The element relative thicknesses of the plies were set as 1, which means they possess the same thickness.

Taking into consideration the computational cost, an explicit analysis is suitable for high-velocity nonlinear problems, such as impact and explosion. This is because their period is extremely short (less than a microsecond). However, in this study, to obtain a higher-resolution spectrum, a motion of at least 0.1 s is required; hence, implicit analysis is more appropriate. The implicit dynamic analysis using direct integration, *Dynamic Implicit* step, was chosen. because the other implicit dynamic steps, while being faster, cannot calculate complex contact nonlinearity problems. In ABAQUS, the Newmark method is the core algorithm that proceeds the *Dynamic Implicit* step, which can refresh the stiffness matrix in every increment to simulate the time-dependence of a nonlinear system.

3.2 Flowchart of the UINTER subroutine

The UINTER subroutine was selected to introduce the modified GW model to control the delamination contact interaction. It is an interface that allows the users to program their own specific contact model to define the contact stiffness K_c. Its principle follows the penalty method, which allows a limited penetration between master and slave surfaces to simulate the contact relative displacement. A certain penetration was input into UINTER to calculate the corresponding contact stress. The UINTER was called for every contact node pair. The contact stress vector and stiffness matrix, named as *STRESS* and *DDSDDR* in UINTER, should be updated after every increment. Fig. 7 illustrates the flowchart of the UINTER process, and the main steps are as follows:

(1) Assuming that the UINTER is executing the (k+1)-th increment, the ABAQUS main program (Black dotted frame) passes the ***statev***(1) (the last residue of dividing by the ABAQUS-assigned k-th increment Δt_k), ***statev***(2) (the number of the last k-th increment), ***statev***(3) (the expected increment, Δt_1), a increment correction fraction r_p, Δt_{k+1} and the normal and tangential relative displacement components in the contact δ s_1 and s_2 into the UINTER subroutine, where the ***statev*** is preset as ***0***.

(2) The UINTER subroutine contains two parts. In the first part, due to the requirement of computational stability of the FEM model and execution convenience of signal processing, an increment control routine (within the red dotted frame) is presented to obtain equal interval increments. This routine firstly exams whether the increment is the first ($k=0$ and ***statev***(2)=0) or second ($k=1$), of which the Δt is naturally equal to the expected increment and assigned to *inc* and ***statev***(3). The ***statev***(2)=0 is not superfluous since the ***statev***(1) is initially smaller than Δt_1 ($k=0$), which will cause the infinite loop. Then, the Δt_{k+1} will be reassigned by assigning the new r_p if the ***statev***(1) is smaller than the Δt_{k+1}, which indicates the Δt_{k+1} has missed the expected time step (integer multiples of the expected increment). Otherwise, the Δt_{k+1} is applied to the next routine.

(3) When the updated increment is qualified, the contact pressure updating routine

(within the blue dotted frame), i.e., the second part of UINTER, determines whether the current contact node pair is open. If it is not open, the current *STRESS* and *DDSDDR* are updated by the calculated P_c, τ_{c1}, τ_{c2} and K_c, $K_{c,T1}$, $K_{c,T2}$; otherwise, they are set as 0. All the (k+1)-th information is stored in ***statev*** to prepare for the next increment calculation. Finally, the updated *STRESS*, *DDSDDR*, and ***statev*** are transferred back to the ABAQUS main program.

4 Experimental procedure

4.1 Specimens and experimental methods

The material used for specimen manufacturing was T300/7901 (Weihai Guang Wei Carbon Fiber Co., Ltd., China), and its mechanical properties are shown in Table 2. The layer-up of the specimens was $[0^{\circ}/90^{\circ}_{2}/0^{\circ}_{2}/90^{\circ}_{2}/0^{\circ}]_{s}$ with a size of 310.0mm×30.0mm×2.1mm, while the cantilever was 250 mm. Delamination was preset at two locations along the thickness direction, namely, the fourth-fifth interlayer for offset delamination and the eighth-ninth interlayer for central delamination. Both delamination locations are the typical damage that may occur when the composite structure is loaded with predominant bending, especially the central delamination which lies in the neutral line, where the significant out-plane stress exists. In total, three delamination sizes of 12.5 mm, 25 mm, and 50 mm were chosen, as seen in Fig. 8. An intact plate was tested as the control case. Since the roughness of the delamination area is a critical factor in determining the parameters of the modified GW model, a re-solidification process was utilized to produce the real delamination. In the first solidification phase, a Teflon film was placed at one end of the composite plate to form the initial delamination. Then, a mode-I load was applied to expand the initial delamination to generate real delamination. There was a fixer, at the other end, to prohibit any further propagation of the real delamination. Finally, an epoxy film was applied to the initial delamination to re-solidity and close it. In total, 4 piezoelectrics (PZT) sheets were fixed on the surface of each specimen, and the locations are indicated in Fig. 9.

Fig. 10 displays the experimental system. The experiments were performed on a vibration isolation table. A signal generator (Tektronix® AFG 3102) was used to provide two sinusoidal signals. One signal was amplified by a power amplifier (DH5871) and passed into a shaker (SH40020) to excite the pump vibration. The other signal was input to the PZT to generate probe waves. The responses were sampled by a digital oscilloscope (Tektronix® DPO 3034) and recorded by the Tektronix® OpenChoice software. Preliminary tests were conducted to determine the LFs and HFs, where 1000-2500 Hz modal frequencies with the strongest harmonic were chosen as LFs and 20-50 kHz frequencies with the maximum amplitude were chosen as HFs. The results are shown in Table 3. It can be noticed that the modes excited by different frequencies may not be the same. However, using the different modes for some cases does not matter here, as long as they can provide a strong enough nonlinear response.

4.2 Signal decoupling

Based on the analysis in Section 2.1, both AMs and FMs exist in the nonlinear acoustic response. Therefore, in order to analyze them separately, a pre-filtered Hilbert Transform (HT) was utilized to decouple the original signal [31]. The procedure of the signal decoupling method is as follows:

(1) The original time-domain signal was transformed into a spectrum by fast Fourier transform (FFT) to determine the highest-order k of the observable sidebands.

(2) A bandpass filter was used to filter out every observable sideband and HF response.

(3) The filtered signal is processed by HT to obtain the amplitude envelope and the instantaneous frequency.

(4) FFT was used to obtain the amplitude of every order harmonic in the amplitude envelope and the instantaneous frequency, $A_{A,i}$ and $A_{F,i}\left(i=1,2,\cdots,k\right)$, respectively.

$A_{A,i}$ and $A_{F,i}$ can be summarized as two nonlinear damage indexes, i.e. the sum of amplitude modulation index (SAMI) and the sum of frequency modulation index (SFMI):

$$SAMI = 20\log\frac{\sum_{i=1}^{k} A_{A,i}}{A_H};\quad SFMI = 20\log\frac{\sum_{i=1}^{k} A_{F,i}}{f_H} \tag{20}$$

where A_H and f_H are the amplitude and frequency of the HF response, respectively.

In addition, due to the lock of method for conducting spatial nonlinear shape decomposition, the sideband index (SBI, similar as the SB_2 in Ref. [27]), was selected to image the damage. The detailed decoupling flowchart of SBI will be presented in Section 5.3.

5 Results and discussion

5.1 Frequency and time domain characteristics

Taking the offset 12.5 mm delaminated composite plate as an example, the typical frequency spectrums of damaged and intact composite plates are presented in Fig. 11. Both the experimental and FEM results of the damaged plates exhibit harmonic and VAM responses. For the experimental result of the intact plate, there were few and weaker nonlinear signals, which may be generated by the excitation system and boundary condition nonlinearities. As for the FEM result of the intact plate, there is no nonlinear response, since the excitation and boundary conditions in FEM are ideal. Under this circumstance, the experimental values of SAMI and SFMI were obtained by subtracting the intact plate results from those of the damaged one.

Fig. 12 displays the time-domain transformation results of pre-filtered HT. The original time-domain shows mainly two fundamental frequencies and can hardly reflect any nonlinear response. As the filtered spectrum illustrates, the noise in experiment, the structural inherent response in FEM, LF, and its harmonics were filtered out, and only the HF and its sidebands remained. Some slight fluctuations in the filtered time-domain appeared but they were not significant, therefore HT was used to extract these slight signals hiding in the HF. Both the experimental and FEM results revealed the existence of AMs and FMs. As shown in Fig. 11 b1), because there are just 4 order sidebands calculated out in the FEM, the numerical AM and FM signal contain fewer higher frequency components, resulting in being different from the experimental one. The same reason also responses the much weak amplitudes of higher-order (>4-th) numerical AMs and FMs, as shown in Fig. 13. These phenomena suggest that the maximum order the proposed FE-model can accurately simulate is the 4-th order. Despite the deviations in higher-order sidebands, the FE-model in this study has been superior compared with former phenomenological quadratic models which usually just provide second or third order precision by manually adding high-order items. In addition, the frequency components of AM and FM consisted of the integral multiples of LF, this is similar to the harmonic.

In this study, making the numerical results perfectly matching the experimental ones is not what the study is intended to, which is relatively difficult for dynamic issues. Three progresses have been achieved and superior to previous simulations: 1) obtain the higher-order (at least 4-th) sidebands without artificially adding high-level items in the contact model, 2) the odd-even order sidebands difference and 3) the asymmetric sidebands suggesting the existence of FM. All three phenomena have been observed in numerous reported experiments, but with little theoretical and simulation explanation before. As long as the above phenomena are displayed, the value of this simulation method is presented.

5.2 Contact behavior

As emphasized in Section 2, contact plays a critical role in the VAM generation. While it is hard to observe such contact experimentally, FEM can help to provide some insight. Two cases with significant contact effects, i.e., the offset and central 50 mm delamination cases, were taken as examples, to determine the contact behavior within an LF circle. The results are shown in Fig. 14, where the contact pressure maps of the 4 phases of LF are displayed. In general, the offset delamination caused much greater contact pressure than the central one, about 1.2×10^{-6} vs. 1.5×10^{-9} MPa, respectively. This is also supported by the greater VAM response in the offset 50 mm case compared to that in the central 50 mm one. Moreover, the difference of the odd-even order sidebands shown in the central 50mm case is larger than that in the offset 50mm case, accompanying more marked amplitude asymmetry, as the blue dot lines display (taking the third-order sidebands as an example). As the amplitude asymmetry is the sign of the existence of FM, it suggests that FM can be used to identify the strength of the contact behavior. In general, the maximum contact pressure occurs at the phase corresponding to the peak of the amplitude envelope, while the valley corresponds to the opening of the interfaces. Due to the geometric symmetry about the delamination, which allows the vibration has the mirrored shapes about the original neutral line in the first and second half-cycles, hence these two half-cycles contact stress distributions of the central 50 mm case are analogous. In some previous simulations, such as Ref. [41], the impact loading was applied to the delaminated composite structure. In the condition of this study, the excitation is steady-state excitation which can be treated as the integration of a series of impact loading. Hence, the signals and contact stress under these two situations are different, where they are attenuated in Ref. [41], but steady and periodic in this study. The same point is both contact behaviors of two excitation conditions are partial and displaying as small impact loadings since the open-close switching is ultrafast.

5.3 Nonlinear DIs

After obtaining the amplitude of each order of harmonics in AM and FM using the pre-filtered HT, the values of SAMI and SFMI can be calculated. Fig. 15 presents the experimental and FEM results of SAMI and SFMI for the 6 delaminated composite plates, including the data concerning the 3 sampling points. The SAMI and SFMI trends predicted by FEM are basically consistent with the experimental ones, which suggests that the FEM method can reflect the actual generation mechanism of VAM to a certain extent. The error between FEM and experimental results could be caused by multiple factors. From the experimental aspect, due to the second solidification, the grade of the embedded epoxy resin film is different from the prepreg epoxy, which may induce local mechanical property discontinuity that generates slight material nonlinearity and increase the DIs. However, the precise effects of this discontinuity on AM and FM are still unknown and remain further investigation. In addition, the thickness of the epoxy resin film may have slightly opened the delamination and decreased the contact strength, since the initial space between two interfaces is extended that should have been ideally 0. As a result, the DIs may be weakened. Although the effects of the different grades of epoxy and the thickness of the film is opposite, it does not mean they can cancel each other out. From the FEM perspective, due to the limitations in calculation capability, the density of the finite element mesh was set to satisfy the minimum requirements, i.e. 8-10 elements per wavelength. At present, the DI magnitude and change trend are close to that of the experiment, which indicates the qualitative effectiveness of the presented FEM.

The results of 4 cases exhibited a positive slope between delamination size and DIs, while those of the other two cases did not. This means that both SAMI and SFMI can characterize the degree of damage when the sampling point location has been appropriately selected. Moreover, in 4 cases, a1) a3) b1) and b2), the slopes of SFMI change are slightly steeper than those of SAMI, especially from the 5%~10% delamination, suggesting that SFMI is more sensitive when the delamination is small. The two non-monotonic cases suggest that there could be a certain spatial distribution of DIs.

The following discussion will focus on the damage imaging using SBI. The procedure to obtain the spatial distribution of DIs is shown in Fig. 16. Firstly, the vibration shapes excited by HF and LF, single HF, and single LF were extracted separately. Subsequently, the two single shapes were subtracted from the combined one to remove the LF and HF responses and their harmonics. The remaining shape is the pure modulation shape. Finally, the maximum amplitude of the modulation shape was recorded and divided by that of the HF response, and the SBI spatial distribution was obtained. Fig. 17

illustrates all the SBI spatial distributions of the 6 delaminated composite plates calculated by FEM. Different from conventional indices that identify damage location via local maximum, SBI utilizes the spatial distribution difference between the delamination and the delamination-free areas. As seen in Fig. 17, appearance of the local maxima of SBI cannot determine the existence of the damage. While there is a significant difference of SBI spatial distribution outlining the delamination boundary precisely, which highly indicates its potential in delamination imaging. One index that can quantitatively characterize the distribution difference is the peak density, i.e., the number of the peaks per unit length. As shown in Table 4, all the peak densities of the delamination areas are higher than the delamination-free area. What's more, the difference between the peak densities of delamination and intact areas is relatively greater when the visual difference of the distribution is more notable. Some linear-feature-based SHM methods can be used to roughly visualize delamination, e.g., the scattering of Lamb waves. However, their visualization capability is based on the precondition that the length of the probe wave is much shorter than the feature size of delamination; otherwise, the probe wave may directly overpass delamination. On the other hand, VAM is not limited by that as the length of the probe wave is allowed to be longer than the feature size of delamination (12.5 mm and 25 mm cases), because the nonlinear features are related to the nonlinear frequency components which wavelength can be shorter than the one of the probe wave.

This imaging method has some disadvantages. Two evident trends can be seen in Fig. 17: the imaging quality decreases with smaller delamination or deeper delamination location in the thickness direction. Two aspects for improving the spatial resolution of this imaging method should be further considered. A generic method is using higher-frequency probe excitations. However, the higher frequency comes up with stronger dispersion and lower signal-to-noise ratio that may cause difficulty in nonlinear decoupling and identification. Even in linear-feature-based methods, strong dispersion and lower signal-to-noise ratio are also troublesome. In addition, the time cost of current nonlinear dynamic FEM is too heavy to simulate the modulation with higher frequency probe excitation. Therefore, the nonlinear dynamic simulation method should be improved specifically for modulation. Beside increasing probe frequency, another method is to use a sharper nonlinear imaging DI. If there is a decomposition method for extracting SAMI and SFMI special distribution, they are expected to replace SBI for sharper damage imaging.

At present, it is only the numerical SBI distributions that are presented. The current PZT-based acquisition system we have is not capable enough to scan the whole plate to obtain the experimental SBI distributions, as the size of the PZT sensor is too large to conduct the high areal density sampling. A possible verification may be achieved via using the laser vibrometer which can provide micron-level sampling point size and automatically scans the whole surface. At least, in this study, we provide the numerical result to show the potential. The verification is being considered for our next-stage work.

6 Conclusions

In this paper, a theoretical analysis and a FEM model for investigating the generation of VAM in delaminated composite plates is presented. The theory is based on a physical CAN model involving a modified GW model and clapping/rubbing discontinuity introduced into FEM via UINTER subroutine, which governs the contact behavior of the delamination interfaces. Every parameter of the modified GW model was determined from microscopic observation rather than fitting experimental data. The simulated VAM results were verified by confirmatory experiments. The main conclusions of this investigation are drawn as follows:

(1) By introducing GW model into FEM via UINTER subroutine, the asymmetry and odd-even difference of sidebands predicted in theory were confirmed, which indicates the simultaneous existence of AM and FM. The odd-even order sidebands difference is related to the strength of contact. Concerning the SAMI and SFMI, the simulated single-point sampling results can approximately reflect the trend of the experimental results. This comparison showed there was still some deviation between the two results, but their order of magnitude was equal. Basically, the proposed FEM method can provide a reasonable approximation of the experimental results.

(2) FEM CPRESS results display strong proof of the existence of the opening and closing phases during a vibration cycle. What is more, they indicate the contact of the interfaces is partial, which may be the reason that frequency modulation exists. The SAMI and SFMI were extracted in both experimental and FEM time-domain signals. Their results generally supported the positive relationship between delamination size and DIs. While SFMI displayed a better sensitivity for detecting smaller delamination.

(3) Some non-monotonic DI results indicate the existence of the spatial distribution of DIs. The SBI spatial distributions for all 6 cases were simulated, demonstrating significantly visual differences in the SBI spatial distributions between the delaminated area and the intact area. A simple index, the peak density, is used to provide a quantification comparison for the SBI distribution difference. The

delamination area’s peak density is higher than intact area. One point that is attractive is this method does not require selecting a probe wave with a wavelength longer than the feature size of delamination, while linear-feature-based methods do. This advantage may benefit the subwavelength delamination and cracks detection.

(4) The proposed damage imaging method provides a blurred result for the Central 12.5mm specimen, indicating it is still limited by the delamination’s depth and size. Further investigation should be conducted via proposing an effective modulation simulation method for increasing the probe frequency, or a spatial decomposition approach for extracting sharper nonlinear damage indices like spatial SAMI and spatial SFMI.

Acknowledgements

This research was funded by the National Natural Science Foundation of China (Grant No.11832014) and Hitachi Construction Machinery Co. Ltd. (Japan) as a part of a project on high strength steel fatigue (HSSF) characteristics (1330-239-0009). The authors want to thank Melody from Imperial College London for conducting the proof reading.

Appendix I: Analytical expression of terms in the differential dynamic function

The terms comprising Eq. (3) are analytically expressed as follows:

$$
\begin{aligned}
& M_x=\rho\phi_x, M_{x0}=\rho\phi_{x0}, M_y=\rho\phi_y, M_{y0}=\rho\phi_{y0}, M_z=\rho\phi_z, M_{z0}=\rho\phi_{z0};\\
& K_x=-\left(\left\{\overline{C}\right\}_1\frac{\partial\boldsymbol{\Phi}}{\partial x}+\left\{\overline{C}\right\}_4\frac{\partial\boldsymbol{\Phi}}{\partial y}+\left\{\overline{C}\right\}_5\frac{\partial\boldsymbol{\Phi}}{\partial z}\right);\\
& K_{x0}=-\left(\left\{\overline{C}\right\}_1\frac{\partial\boldsymbol{\Phi}_0}{\partial x}+\left\{\overline{C}\right\}_4\frac{\partial\boldsymbol{\Phi}_0}{\partial y}+\left\{\overline{C}\right\}_5\frac{\partial\boldsymbol{\Phi}_0}{\partial z}\right);\\
& K_y=-\left(\left\{\overline{C}\right\}_4\frac{\partial\boldsymbol{\Phi}}{\partial x}+\left\{\overline{C}\right\}_2\frac{\partial\boldsymbol{\Phi}}{\partial y}+\left\{\overline{C}\right\}_6\frac{\partial\boldsymbol{\Phi}}{\partial z}\right);\\
& K_{y0}=-\left(\left\{\overline{C}\right\}_4\frac{\partial\boldsymbol{\Phi}_0}{\partial x}+\left\{\overline{C}\right\}_2\frac{\partial\boldsymbol{\Phi}_0}{\partial y}+\left\{\overline{C}\right\}_6\frac{\partial\boldsymbol{\Phi}_0}{\partial z}\right);\\
& K_z=-\left(\left\{\overline{C}\right\}_5\frac{\partial\boldsymbol{\Phi}}{\partial x}+\left\{\overline{C}\right\}_6\frac{\partial\boldsymbol{\Phi}}{\partial y}+\left\{\overline{C}_{31}\quad\overline{C}_{32}\quad K_c\quad\overline{C}_{34}\quad\overline{C}_{34}\quad\overline{C}_{35}\right\}\frac{\partial\boldsymbol{\Phi}}{\partial z}\right);\\
& K_{z0}=-\left(\left\{\overline{C}\right\}_5\frac{\partial\boldsymbol{\Phi}_0}{\partial x}+\left\{\overline{C}\right\}_6\frac{\partial\boldsymbol{\Phi}_0}{\partial y}+\left\{\overline{C}_{31}\quad\overline{C}_{32}\quad K_c\quad\overline{C}_{34}\quad\overline{C}_{34}\quad\overline{C}_{35}\right\}\frac{\partial\boldsymbol{\Phi}_0}{\partial z}\right);\\
& \boldsymbol{\Phi}=\left\{\frac{\partial\phi_x}{\partial x}\quad\frac{\partial\phi_y}{\partial y}\quad\frac{\partial\phi_z}{\partial z}\quad\frac{\partial\phi_y}{\partial x}+\frac{\partial\phi_x}{\partial y}\quad\frac{\partial\phi_z}{\partial x}+\frac{\partial\phi_x}{\partial z}\quad\frac{\partial\phi_y}{\partial z}+\frac{\partial\phi_z}{\partial y}\right\}^T;\\
& \boldsymbol{\Phi}_0=\left\{\frac{\partial\phi_{x0}}{\partial x}\quad\frac{\partial\phi_{y0}}{\partial y}\quad\frac{\partial\phi_{z0}}{\partial z}\quad\frac{\partial\phi_{y0}}{\partial x}+\frac{\partial\phi_{x0}}{\partial y}\quad\frac{\partial\phi_{z0}}{\partial x}+\frac{\partial\phi_{x0}}{\partial z}\quad\frac{\partial\phi_{y0}}{\partial z}+\frac{\partial\phi_{z0}}{\partial y}\right\}^T;\\
& \boldsymbol{M}=diag\left(M_x,M_y,M_z\right), \boldsymbol{M}_0=diag\left(M_{x0},M_{y0},M_{z0}\right);\\
& \boldsymbol{K}=diag\left(K_x,K_y,K_z\right), \boldsymbol{K}_0=diag\left(K_x,K_y,K_{z0}\right), \boldsymbol{q}=\left\{q\ q\ q\right\}^T;
\end{aligned}
\tag{I-1}
$$

where $\left\{\overline{C}\right\}_i, \left(i=1,\cdots,6\right)$ refers to i-th row vector of the transformed stiffness matrix of composite material $\overline{\boldsymbol{C}}$, and elements of the excitation vector $\boldsymbol{F}=\left\{\overline{F}_x\ \overline{F}_y\ \overline{F}_z\right\}^T$ are:

$$
\overline{F}_x=\left(\frac{\partial\overline{f}_{xx}}{\partial x}+\frac{\partial\overline{f}_{yx}}{\partial y}+\frac{\partial\overline{f}_{zx}}{\partial z}\right);\ \overline{F}_y=\left(\frac{\partial\overline{f}_{xy}}{\partial x}+\frac{\partial\overline{f}_{yy}}{\partial y}+\frac{\partial\overline{f}_{zy}}{\partial z}\right);\ \overline{F}_z=\left(\frac{\partial\overline{f}_{xz}}{\partial x}+\frac{\partial\overline{f}_{yz}}{\partial y}+\frac{\partial\overline{f}_{zz}}{\partial z}\right)
\tag{I-2}
$$

Appendix II: Derivation for determining the third element expression of Eq.(8)

By substituting Eq.(10) into Eq.(8), the third element of Eq.(8) can be expressed as:

$$
\begin{aligned}
&\frac{\partial^2\phi_z}{\partial z^2}\left(K_c-\overline{C}_{33}\right)\left(\sin\left(\omega_1 t+\theta_1\right)+\sin\left(\omega_2 t+\theta_2\right)\right)\\
&=\frac{\partial^2\phi_z}{\partial z^2}\left(\left(\frac{k_{a,0}}{2}-\overline{C}_{33}\right)+\sum_{n=1}^{\infty}\left(k_{a,n}\cos\left(n\omega t\right)+k_{b,n}\sin\left(n\omega t\right)\right)\right)\left(\sin\left(\omega_1 t+\theta_1\right)+\sin\left(\omega_2 t+\theta_2\right)\right)\\
&=\frac{\partial^2\phi_z}{\partial z^2}\left(\begin{array}{l}\underbrace{\left(\frac{k_{a,0}}{2}-\overline{C}_{33}\right)\left(\sin\left(\omega_1 t+\theta_1\right)+\sin\left(\omega_2 t+\theta_2\right)\right)}_{\mathrm{I}}\\
\qquad+\underbrace{\left(\sin\left(\omega_1 t+\theta_1\right)+\sin\left(\omega_2 t+\theta_2\right)\right)\sum_{n=1}^{\infty}\left(k_{a,n}\cos\left(n\omega t\right)+k_{b,n}\sin\left(n\omega t\right)\right)}_{\mathrm{II}}\end{array}\right)
\end{aligned}
\tag{II-1}
$$

The part II can be further expanded by using trigonometric identities:

$$
\begin{aligned}
&\left(\sin\left(\omega_1 t+\theta_1\right)+\sin\left(\omega_2 t+\theta_2\right)\right)\sum_{n=1}^{\infty}\left(k_{a,n}\cos\left(n\omega t\right)+k_{b,n}\sin\left(n\omega t\right)\right)\\
&=\sum_{n=1}^{\infty}\left(k_{a,n}\cos\left(n\omega t\right)+k_{b,n}\sin\left(n\omega t\right)\right)\left(\sin\left(\omega_1 t+\theta_1\right)+\sin\left(\omega_2 t+\theta_2\right)\right)\\
&=\sum_{n=1}^{\infty}\left(\begin{array}{l}k_{a,n}\sin\left(\omega_1 t+\theta_1\right)\cos\left(n\omega t\right)+k_{a,n}\sin\left(\omega_2 t+\theta_2\right)\cos\left(n\omega t\right)+\\
k_{b,n}\sin\left(\omega_1 t+\theta_1\right)\sin\left(n\omega t\right)+k_{b,n}\sin\left(\omega_2 t+\theta_2\right)\sin\left(n\omega t\right)\end{array}\right)\\
&=\frac{1}{2}\sum_{n=1}^{\infty}\left(\begin{array}{l}k_{a,n}\left(\sin\left(\left(\omega_1+n\omega\right)t+\theta_1\right)+\sin\left(\left(\omega_1-n\omega\right)t+\theta_1\right)\right)+\\
k_{a,n}\left(\sin\left(\left(\omega_2+n\omega\right)t+\theta_2\right)+\sin\left(\left(\omega_2-n\omega\right)t+\theta_2\right)\right)+\\
k_{b,n}\left(\cos\left(\left(\omega_1-n\omega\right)t+\theta_1\right)-\cos\left(\left(\omega_1+n\omega\right)t+\theta_1\right)\right)+\\
k_{b,n}\left(\cos\left(\left(\omega_2-n\omega\right)t+\theta_2\right)-\cos\left(\left(\omega_2+n\omega\right)t+\theta_2\right)\right)\end{array}\right)\\
&=\frac{1}{2}\sum_{n=1}^{\infty}\left(\begin{array}{l}\left(k_{a,n}\sin\left(\left(\omega_1+n\omega\right)t+\theta_1\right)-k_{b,n}\cos\left(\left(\omega_1+n\omega\right)t+\theta_1\right)\right)+\\
\left(k_{a,n}\sin\left(\left(\omega_1-n\omega\right)t+\theta_1\right)+k_{b,n}\cos\left(\left(\omega_1-n\omega\right)t+\theta_1\right)\right)+\\
\left(k_{a,n}\sin\left(\left(\omega_2+n\omega\right)t+\theta_2\right)-k_{b,n}\cos\left(\left(\omega_2+n\omega\right)t+\theta_2\right)\right)+\\
\left(k_{a,n}\sin\left(\left(\omega_2-n\omega\right)t+\theta_2\right)+k_{b,n}\cos\left(\left(\omega_2-n\omega\right)t+\theta_2\right)\right)\end{array}\right)\\
&=\frac{1}{2}\sum_{n=1}^{\infty}\left(\sqrt{k_{a,n}^2+k_{b,n}^2}\left(\begin{array}{l}\sin\left(\left(\omega_1+n\omega\right)t+\theta_1-\theta_n\right)+\\
\sin\left(\left(\omega_1-n\omega\right)t+\theta_1+\theta_n\right)+\\
\sin\left(\left(\omega_2+n\omega\right)t+\theta_2-\theta_n\right)+\\
\sin\left(\left(\omega_2-n\omega\right)t+\theta_2+\theta_n\right)\end{array}\right)\right),\left(\tan\theta_n=k_{b,n}/k_{a,n}\right)
\end{aligned}
\tag{II-2}
$$

Combining Eq.(II-1) and Eq.(II-2), the third element of Eq.(8) can be obtained as shown in Eq.(11).

Appendix Ⅲ: Derivation for first-order sidebands

The first-order sideband frequency components are $\omega_2 \pm \omega_1$. Based on Eq.(9) and Eq.(11), the n corresponding to $\omega_2+\omega_1$ and $\omega_2-\omega_1$ are j and k. Then, for $\omega_2+\omega_1$ component, the amplitude can be derived out by using trigonometric identities:

$$\begin{aligned}
&\frac{1}{2}\left(\frac{\partial^2\phi_z}{\partial z^2}\right)\left(\sqrt{k_{a,j}^2+k_{b,j}^2}\sin\left((\omega_2+j\omega)t+\theta_2-\theta_j\right)+\sqrt{k_{a,k}^2+k_{b,k}^2}\sin\left((\omega_1+k\omega)t+\theta_1-\theta_k\right)\right)\\
&=\frac{1}{2}\left(\frac{\partial^2\phi_z}{\partial z^2}\right)\left(\sqrt{k_{a,j}^2+k_{b,j}^2}\sin\left((\omega_2+\omega_1)t+\theta_2-\theta_j\right)+\sqrt{k_{a,k}^2+k_{b,k}^2}\sin\left((\omega_1+\omega_2)t+\theta_1-\theta_k\right)\right)\\
&=\frac{1}{2}\left(\frac{\partial^2\phi_z}{\partial z^2}\right)\begin{pmatrix}\sqrt{k_{a,j}^2+k_{b,j}^2}\left(\sin\left((\omega_2+\omega_1)t\right)\cos\left(\theta_2-\theta_j\right)+\cos\left((\omega_2+\omega_1)t\right)\sin\left(\theta_2-\theta_j\right)\right)+\\ \sqrt{k_{a,k}^2+k_{b,k}^2}\left(\sin\left((\omega_2+\omega_1)t\right)\cos\left(\theta_1-\theta_k\right)+\cos\left((\omega_2+\omega_1)t\right)\sin\left(\theta_1-\theta_k\right)\right)\end{pmatrix} \quad \text{(III-1)}\\
&=\frac{1}{2}\left(\frac{\partial^2\phi_z}{\partial z^2}\right)\begin{pmatrix}\left(\sqrt{k_{a,j}^2+k_{b,j}^2}\cos\left(\theta_2-\theta_j\right)+\sqrt{k_{a,k}^2+k_{b,k}^2}\cos\left(\theta_1-\theta_k\right)\right)\sin\left((\omega_2+\omega_1)t\right)+\\ \left(\sqrt{k_{a,j}^2+k_{b,j}^2}\sin\left(\theta_2-\theta_j\right)+\sqrt{k_{a,k}^2+k_{b,k}^2}\sin\left(\theta_1-\theta_k\right)\right)\cos\left((\omega_2+\omega_1)t\right)\end{pmatrix}\\
&=A_{\omega_1+\omega_2}\sin\left((\omega_2+\omega_1)t+\theta_{\omega_1+\omega_2}\right)
\end{aligned}$$

where,

$$\begin{aligned}
A_{\omega_1+\omega_2}&=\frac{1}{2}\left(\frac{\partial^2\phi_z}{\partial z^2}\right)\sqrt{A_{\omega_1+\omega_2,1}^2+A_{\omega_1+\omega_2,2}^2}\\
&=\frac{1}{2}\left(\frac{\partial^2\phi_z}{\partial z^2}\right)\sqrt{k_{a,j}^2+k_{b,j}^2+k_{a,k}^2+k_{b,k}^2+2\sqrt{\left(k_{a,j}^2+k_{b,j}^2\right)\left(k_{a,k}^2+k_{b,k}^2\right)}\cos\left(\theta_2-\theta_j-\theta_1+\theta_k\right)}\\
\tan\theta_{\omega_1+\omega_2}&=\frac{A_{\omega_1+\omega_2,2}}{A_{\omega_1+\omega_2,1}} \qquad \text{(III-2)}\\
A_{\omega_1+\omega_2,1}&=\frac{1}{2}\left(\frac{\partial^2\phi_z}{\partial z^2}\right)\left(\sqrt{k_{a,j}^2+k_{b,j}^2}\cos\left(\theta_2-\theta_j\right)+\sqrt{k_{a,k}^2+k_{b,k}^2}\cos\left(\theta_1-\theta_k\right)\right)\\
A_{\omega_1+\omega_2,2}&=\frac{1}{2}\left(\frac{\partial^2\phi_z}{\partial z^2}\right)\left(\sqrt{k_{a,j}^2+k_{b,j}^2}\sin\left(\theta_2-\theta_j\right)+\sqrt{k_{a,k}^2+k_{b,k}^2}\sin\left(\theta_1-\theta_k\right)\right)
\end{aligned}$$

Using the similar derivation, the amplitude of $\omega_2-\omega_1$ component is also obtained:

$$
\begin{aligned}
&A_{\omega_1-\omega_2}\sin\left(\left(\omega_2-\omega_1\right)t+\theta_{\omega_1-\omega_2}\right)\\
&A_{\omega_1-\omega_2}=\frac{1}{2}\left(\frac{\partial^2\phi_z}{\partial z^2}\right)\sqrt{A_{\omega_1-\omega_2,1}^2+A_{\omega_1-\omega_2,2}^2}\\
&\qquad=\frac{1}{2}\left(\frac{\partial^2\phi_z}{\partial z^2}\right)\sqrt{k_{a,j}^2+k_{b,j}^2+k_{a,k}^2+k_{b,k}^2-2\sqrt{\left(k_{a,j}^2+k_{b,j}^2\right)\left(k_{a,k}^2+k_{b,k}^2\right)}\cos\left(\theta_2+\theta_j+\theta_1+\theta_k\right)}\\
&\tan\theta_{\omega_1+\omega_2}=\frac{A_{\omega_1-\omega_2,2}}{A_{\omega_1-\omega_2,1}}\\
&A_{\omega_1-\omega_2,1}=\frac{1}{2}\left(\frac{\partial^2\phi_z}{\partial z^2}\right)\left(\sqrt{k_{a,j}^2+k_{b,j}^2}\cos\left(\theta_2+\theta_j\right)-\sqrt{k_{a,k}^2+k_{b,k}^2}\cos\left(\theta_1+\theta_k\right)\right)\\
&A_{\omega_1-\omega_2,2}=\frac{1}{2}\left(\frac{\partial^2\phi_z}{\partial z^2}\right)\left(\sqrt{k_{a,j}^2+k_{b,j}^2}\sin\left(\theta_2+\theta_j\right)+\sqrt{k_{a,k}^2+k_{b,k}^2}\sin\left(\theta_1+\theta_k\right)\right)
\end{aligned}
\tag{III-3}
$$

Reference

[1] Su Z, Ye L.Lamb wave-based quantitative identification of delamination in CF/EP composite structures using artificial neural algorithm[J].Composite Structures,2004, 66 (1-4): 627-637.

[2] He Y, Xiao Y, Su Z.Effects of surface contact on the dynamic responses of delaminated composite plates[J].Composite Structures,2019, 229: 111378.

[3] Qian Z. Nonlinear Acoustic[M].Beijing: Science Press,1992.

[4] Hu H. Research on Theory and Key Technologies of Nonlinear Ultrasonics for Health Monitoring of Plate-like Metallic Structures [D].Changsha: National University of Defense Technology 2011.

[5] Zhang Z, Liu M, Liao Y, et al.Contact acoustic nonlinearity (CAN)-based continuous monitoring of bolt loosening: Hybrid use of high-order harmonics and spectral sidebands[J].Mechanical Systems and Signal Processing,2018, 103: 280-294.

[6] Solodov I Y, Krohn N, Busse G.CAN: an example of nonclassical acoustic nonlinearity in solids[J].Ultrasonics,2002, 40 (1-8): 621-625.

[7] Breazeale M, Thompson D.Finite-amplitude ultrasonic waves in aluminum[J].Applied Physics Letters,1963, 3 (5): 77-78.

[8] Breazeale M, Hiedemann E.Investigation of progressive ultrasonic waves by light refraction[J].The Journal of the Acoustical Society of America,1958, 30 (8): 751-756.

[9] Hikata A, Chick B B, Elbaum C.Dislocation contribution to the second harmonic generation of ultrasonic waves[J].Journal of Applied Physics,1965, 36 (1): 229-236.

[10] Buck O, Morris W, Richardson J M.Acoustic harmonic generation at unbonded interfaces and fatigue cracks[J].Applied Physics Letters,1978, 33 (5): 371-373.

[11] Richardson J M.Harmonic generation at an unbonded interface—I. Planar interface between semi-infinite elastic media[J].International Journal of Engineering Science,1979, 17 (1): 73-85.

[12] Morris W, Buck O, Inman R.Acoustic harmonic generation due to fatigue damage in high-strength aluminum[J].Journal of Applied Physics,1979, 50 (11): 6737-6741.
[13] Shkerdin G, Glorieux C.Nonlinear modulation of Lamb modes by clapping delamination[J].The Journal of the Acoustical Society of America,2008, 124 (6): 3397-3409.
[14] Shkerdin G, Glorieux C.Nonlinear clapping modulation of lamb modes by normally closed delamination[J].IEEE transactions on ultrasonics, ferroelectrics, frequency control,2010, 57 (6): 1426-1433.
[15] Soleimanpour R, Ng C-T, Wang C H.Higher harmonic generation of guided waves at delaminations in laminated composite beams[J].Structural Health Monitoring,2017, 16 (4): 400-417.
[16] Soleimanpour R, Ng C-T.Locating delaminations in laminated composite beams using nonlinear guided waves[J].Engineering Structures,2017, 131: 207-219.
[17] Yelve N P, Mitra M, Mujumdar P.Detection of delamination in composite laminates using Lamb wave based nonlinear method[J].Composite Structures,2017, 159: 257-266.
[18] Donskoy D M, Sutin A M.Vibro-acoustic modulation nondestructive evaluation technique[J].Journal of Intelligent Material Systems and Structures,1998, 9 (9): 765-771.
[19] Sutin A M, Donskoy D M: Nonlinear vibro-acoustic nondestructive testing technique,Nondestructive Characterization of Materials VIII: Springer,1998: 133-138.
[20] Duffour P, Morbidini M, Cawley P.A study of the vibro-acoustic modulation technique for the detection of cracks in metals[J].The Journal of the Acoustical Society of America,2006, 119 (3): 1463-1475.
[21] Solodov I, Wackerl J, Pfleiderer K, et al.Nonlinear self-modulation and subharmonic acoustic spectroscopyfor damage detection and location[J].Applied physics letters,2004, 84 (26): 5386-5388.
[22] Meo M, Zumpano G.Nonlinear elastic wave spectroscopy identification of impact damage on a sandwich plate[J].Composite structures,2005, 71 (3-4): 469-474.
[23] Aymerich F, Staszewski W.Experimental study of impact-damage detection in composite laminates using a cross-modulation vibro-acoustic technique[J].Structural Health Monitoring,2010, 9 (6): 541-553.
[24] Aymerich F, Staszewski W.Impact damage detection in composite laminates using nonlinear acoustics[J].Composites Part A: Applied Science and Manufacturing,2010, 41 (9): 1084-1092.
[25] Delsanto P P. Universality of nonclassical nonlinearity[M].New York: Springer,2006.
[26] Chen B-Y, Soh S-K, Lee H-P, et al.A vibro-acoustic modulation method for the detection of delamination and kissing bond in composites[J].Journal of Composite Materials,2016, 50 (22): 3089-3104.
[27] Klepka A, Staszewski W, Jenal R, et al.Nonlinear acoustics for fatigue crack detection–experimental investigations of vibro-acoustic wave modulations[J].Structural Health Monitoring,2012, 11 (2): 197-211.

[28] Klepka A, Staszewski W J, Di Maio D, et al.Impact damage detection in composite chiral sandwich panels using nonlinear vibro-acoustic modulations[J].Smart Materials and Structures,2013, 22 (8): 084011.

[29] Klepka A, Pieczonka L, Staszewski W, et al.Impact damage detection in laminated composites by non-linear vibro-acoustic wave modulations[J].Composites Part B: Engineering,2014, 65: 99-108.

[30] Klepka A, Strączkiewicz M, Pieczonka L, et al.Triple correlation for detection of damage-related nonlinearities in composite structures[J].Nonlinear dynamics,2015, 81 (1-2): 453-468.

[31] Ooijevaar T, Rogge M D, Loendersloot R, et al.Vibro-acoustic modulation–based damage identification in a composite skin–stiffener structure[J].Structural health monitoring,2016, 15 (4): 458-472.

[32] Singh A K, Chen B, Tan V B, et al.A theoretical and numerical study on the mechanics of vibro-acoustic modulation[J].The Journal of the Acoustical Society of America,2017, 141 (4): 2821-2831.

[33] Singh A K, Chen B-Y, Tan V B, et al.Finite element modeling of nonlinear acoustics/ultrasonics for the detection of closed delaminations in composites[J].Ultrasonics,2017, 74: 89-98.

[34] Singh A K, Tan V B, Tay T E, et al.Experimental investigations into nonlinear vibro-acoustics for detection of delaminations in a composite laminate[J].Journal of Nondestructive Evaluation, Diagnostics and Prognostics of Engineering Systems,2019, 2 (1): 011002.

[35] Yoder N C, Adams D E.Vibro-acoustic modulation utilizing a swept probing signal for robust crack detection[J].Structural Health Monitoring,2010, 9 (3): 257-267.

[36] Greenwood J A, Williamson J B P P.Contact of Nominally Flat Surfaces[J].Proceedings of The Royal Society A: Mathematical, Physical and Engineering Sciences,1966, 295 (1442): 300-319.

[37] Adler R J, Firmin D, Kendall D G.A non-Gaussian model for random surfaces[J].Philosophical Transactions of the Royal Society of London. Series A: Mathematical, Physical and Sciences,1981, 303 (1479): 433-462.

[38] Brown S R, Scholz C H.Closure of random elastic surfaces in contact[J].Journal of Geophysical Research: Solid Earth,1985, 90 (B7): 5531-5545.

[39] Baltazar A, Rokhlin S I, Pecorari C.On the relationship between ultrasonic and micromechanical properties of contacting rough surfaces[J].Journal of the Mechanics and Physics of Solids,2002, 50 (7): 1397-1416.

[40] Abaqus V.6.14 Documentation[J].Dassault Systemes Simulia Corporation,2014, 651: 6.2.

[41] Burlayenko V N, Sadowski T.Transient dynamic response of debonded sandwich plates predicted with finite element analysis[J].Meccanica,2014, 49 (11): 2617-2633.

Nomenclature

u, v, w	Displacement components
ϕ_i, $\phi_{i0}\left(i=x,y,z\right)$	Linear and nonlinear modal functions
q, q_0	Linear and nonlinear periodic functions
σ_{ii}, $\tau_{ij}\left(i,j=x,y,z\right)$	Stress components
$\overline{f}_{ij}\left(i,j=x,y,z\right)$	Differential exciting forces components
ρ	Density
M_i, $M_{i0}\left(i=x,y,z\right)$	Linear and nonlinear mass coefficients
K_i, $K_{i0}\left(i=x,y,z\right)$	Linear and nonlinear stiffness coefficients
$\boldsymbol{M}$, $\boldsymbol{M}_0$	Linear and nonlinear mass matrices
$\boldsymbol{K}$, $\boldsymbol{K}_0$	Linear and nonlinear stiffness matrices
$\overline{F}_i\left(i=x,y,z\right)$	Excitation components
$\boldsymbol{F}$	Excitation vector
$\boldsymbol{q}$, $\boldsymbol{q}_0$	Linear and perturbation response vectors
$\overline{\boldsymbol{C}}$	Transformed stiffness matrix of composite material
$\left\{\overline{C}\right\}_i,\left(i=1,\cdots,6\right)$	i-th row vector of $\overline{\boldsymbol{C}}$
K_c	Nonlinear contact stiffness
$\boldsymbol{K}_L$, $\boldsymbol{K}_N$	Sub-matrices of $\boldsymbol{K}$
$\boldsymbol{K}_{L0}$, $\boldsymbol{K}_{N0}$	Sub-matrices of $\boldsymbol{K}_0$
ω_1, ω_2	Circular frequency of the two sinusoidal excitations
θ_1, $\theta_2\left(i=x,y,z\right)$	Phases of the two sinusoidal excitations
F_c	Contact force
E_1, E_2	Elastic moduli of contact materials
R_1, R_2	Radii of the two contact hemispheres
v_1, v_2	Poisson's ratio of contact materials
E^*	Equivalent elastic modulus
R^*	Equivalent radius of the equivalent contact hemisphere
δ	Relative contact displacement
P_c	Normal contact pressure
$K_{c,N}$	Normal contact stiffness
τ_c	Tangential contact shear stress
$K_{c,T}$	Tangential contact stiffness
β	Average radius of the peaks on the rough interfaces
η	Density of peaks on the rough interfaces
G^*	Equivalent shear modulus
G_1, G_2	Shear moduli of contact materials

φ	Height distribution of peaks in the z-direction
n_{chi}	DoF of Chi-squared probability density function
Γ	Gamma function
γ	Normal dislocation angle
α	Tangential dislocation angle

Table and Figure Captions:

Figure 1 VAM generation by local contact in an excited delaminated composite plate (color images in the e-edition, same hereinafter)

Figure 2 Hertz contact model describing the contact behavior between two hemisphere peaks (left) and the equivalent transformation as a contact between a hemisphere peak and a rigid plane (right).

Figure 3 Rough surface and rigid plane equivalent of the contact between rough surfaces.

Figure 4 Dislocation of a contact peak pair.

Figure 5 Microscopic observation of rough delamination interfaces.

Figure 6 Schematic diagram of a 4-DoF system with local nonlinear stiffness.

Figure 7 Spectrum results for a 4-DoF system (a-c) with clapping and (d-e) without clapping.

Figure 8 FEM model of delaminated composite plates: contact pair construction and mesh.

Figure 9 Flowchart of the FEM calculation process combined with the UINTER subroutine. (Black: ABAQUS main program; Red: increment control; Blue: contact pressure updating)

Figure 10 Specimen geometry.

Figure 11 Schematic diagram of a specimen showing the locations of the excitation and sampling points.

Figure 12 Experimental system.

Figure 13 Frequency spectra of the offset 12.5 mm delaminated composite plate and the corresponding intact plate (sampling point 1).

Figure 14 Offset 12.5 mm time-domain transformation procedure results of pre-filtered HT (sampling point 1).

Figure 15 Frequency components of AM and FM in the offset 12.5 mm case (sampling point 1).

Figure 16 Contact pressure contours at different phases on the offset (Left) and central (Right) 50 mm delamination plates and corresponding spectrums.

Figure 17 Predicted and experimentally obtained SAMI and SFMI of the 6 delaminated composite plates.

Figure 18 Procedure for extracting the calculated spatial distribution of SBI.

Figure 19 SBI spatial distribution of the 6 delaminated composite plates.

Table 1 Parameters of the 4-DoF system.

Table 2 Modified GW model parameters

Table 3 Material properties of the T300/7901 carbon/epoxy composites.

Table 4 Selected LFs and HFs.

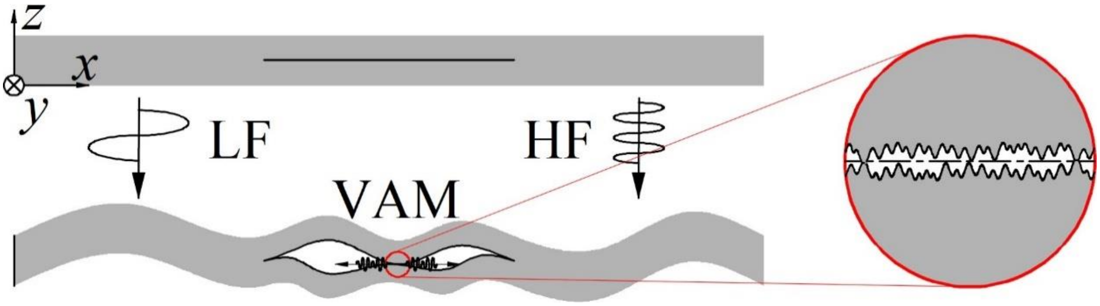

Figure 1 VAM generation by local contact in an excited delaminated composite plate (color images in the e-edition, same hereinafter)

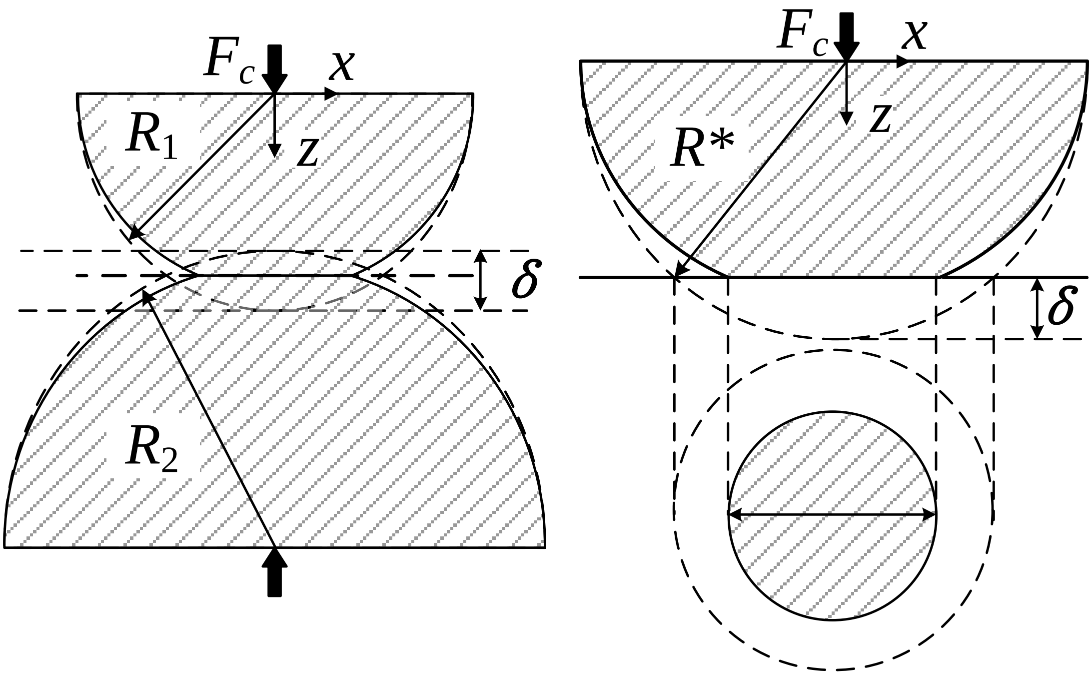

Figure 2 Hertz contact model describing the contact behavior between two hemisphere peaks (left) and the equivalent transformation as a contact between a hemisphere peak and a rigid plane (right).

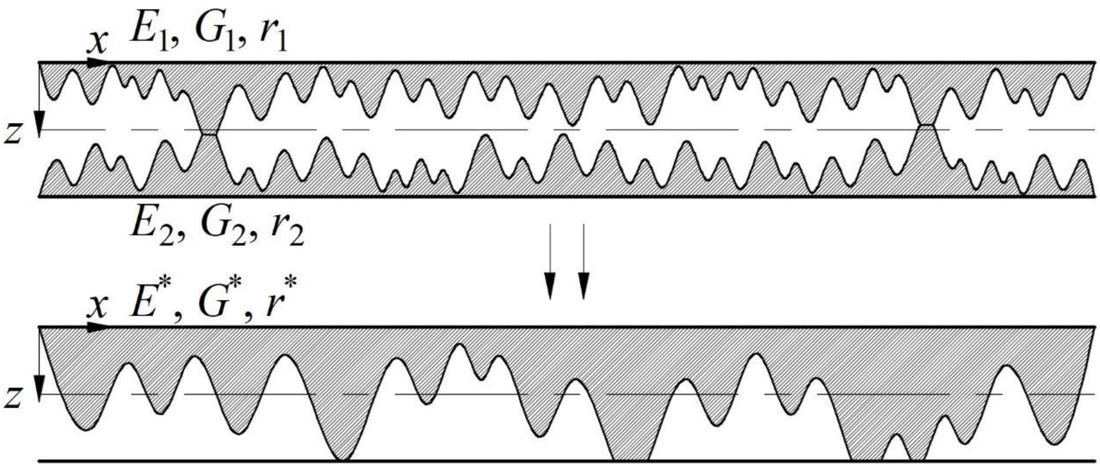

Figure 3 Rough surface and rigid plane equivalent of the contact between rough surfaces.

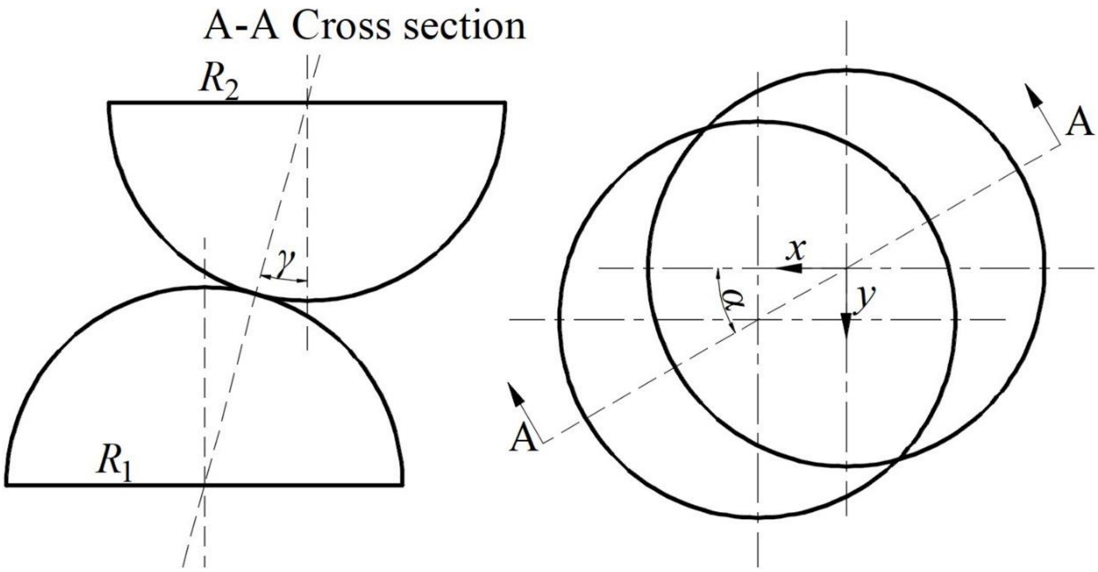

Figure 4 Dislocation of a contact peak pair.

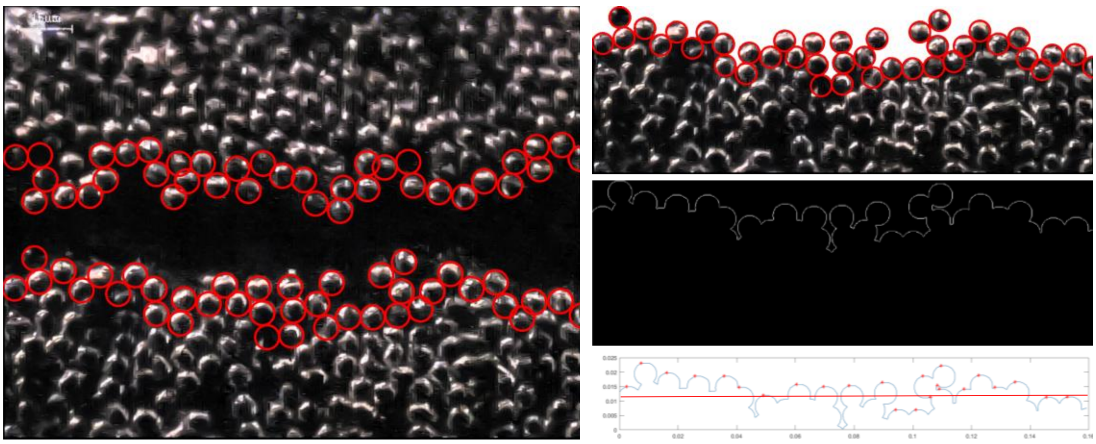

Figure 5 Microscopic observation of rough delamination interfaces.

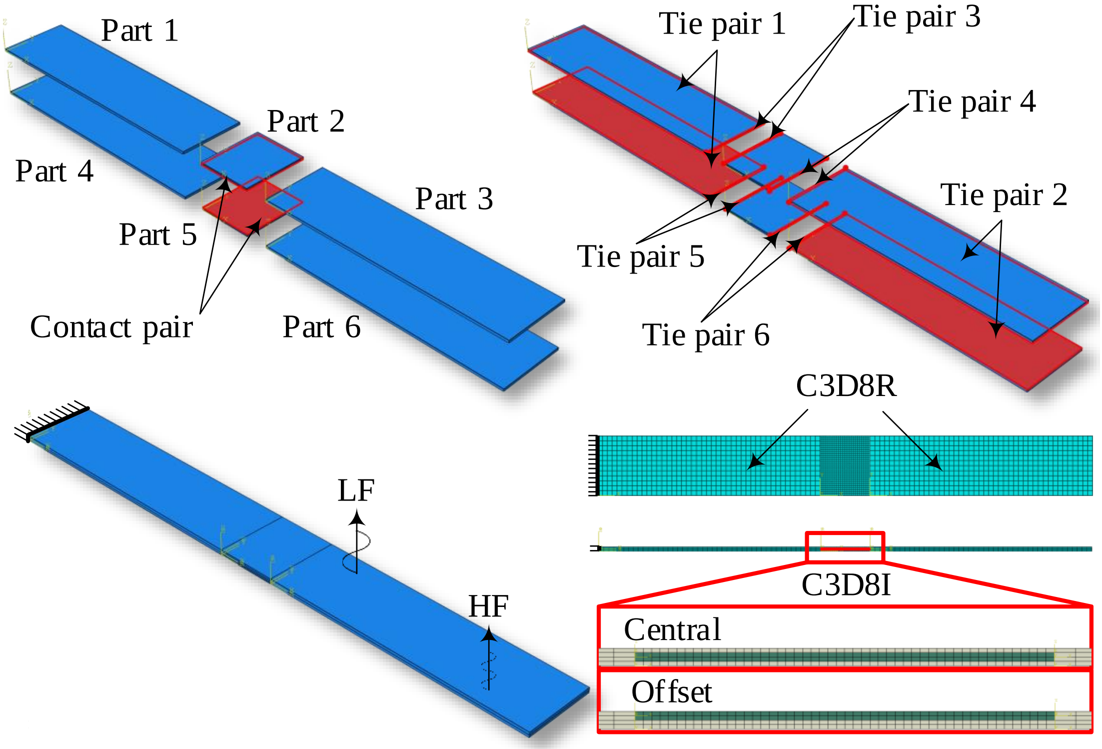

Figure 6 FEM model of delaminated composite plates: contact pair construction and mesh

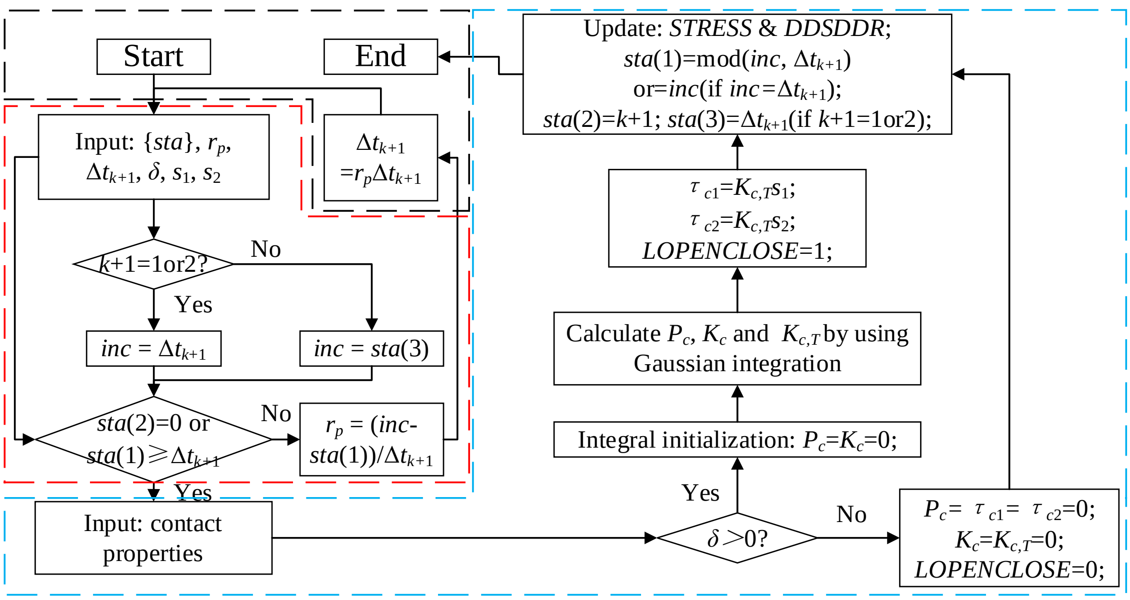

Figure 7 Flowchart of the FEM calculation combined with UINTER subroutine. (Black: ABAQUS main program; Red: increment control; Blue: contact pressure updating)

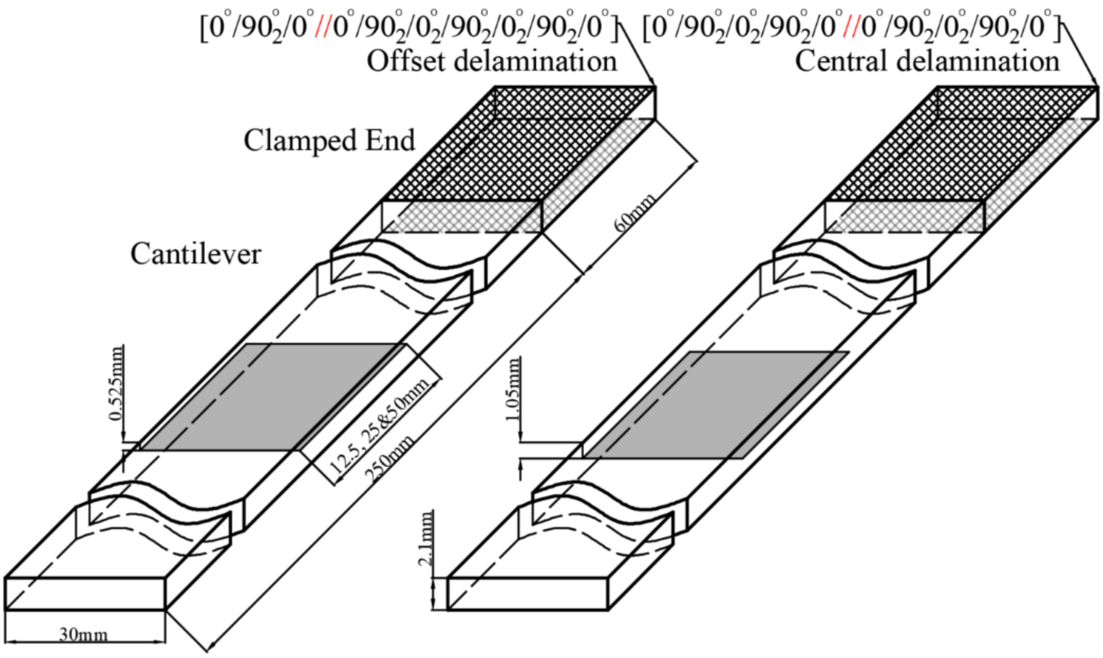

Figure 8 Specimen geometry.

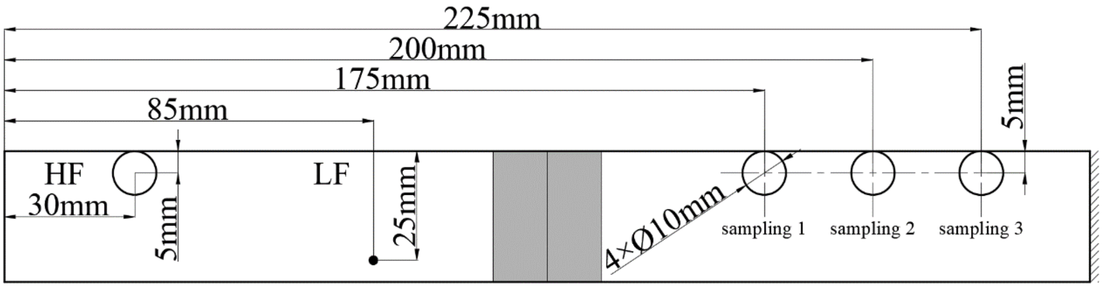

Figure 9 Schematic diagram of a specimen showing the locations of the excitation and sampling points.

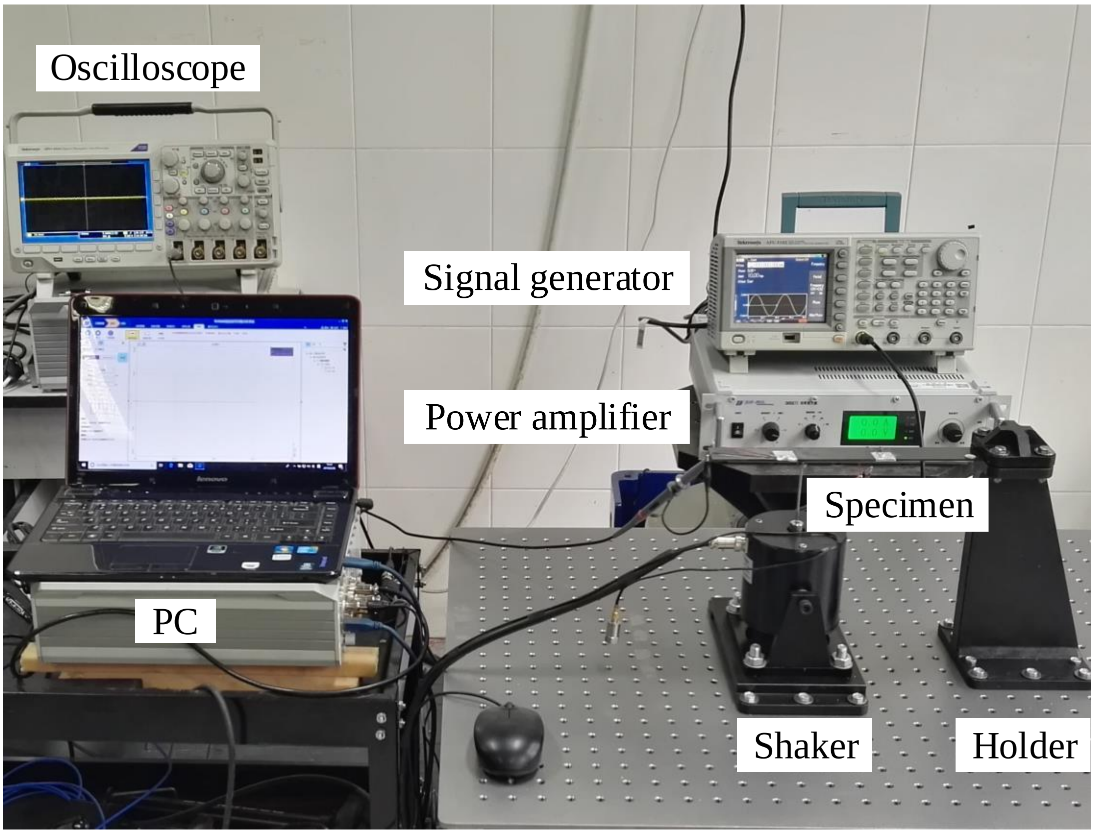

Figure 10 Experimental system.

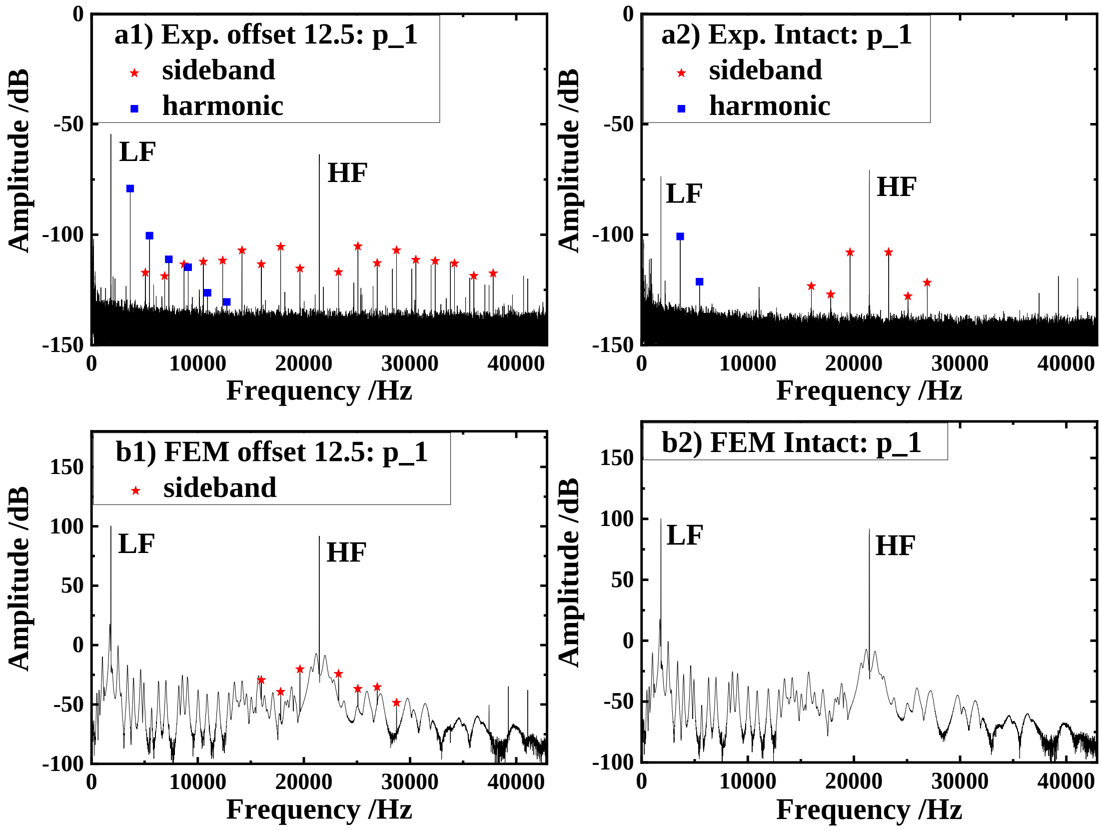

Figure 11 Frequency spectra of the offset 12.5 mm delaminated composite plate and the corresponding intact plate (sampling point 1).

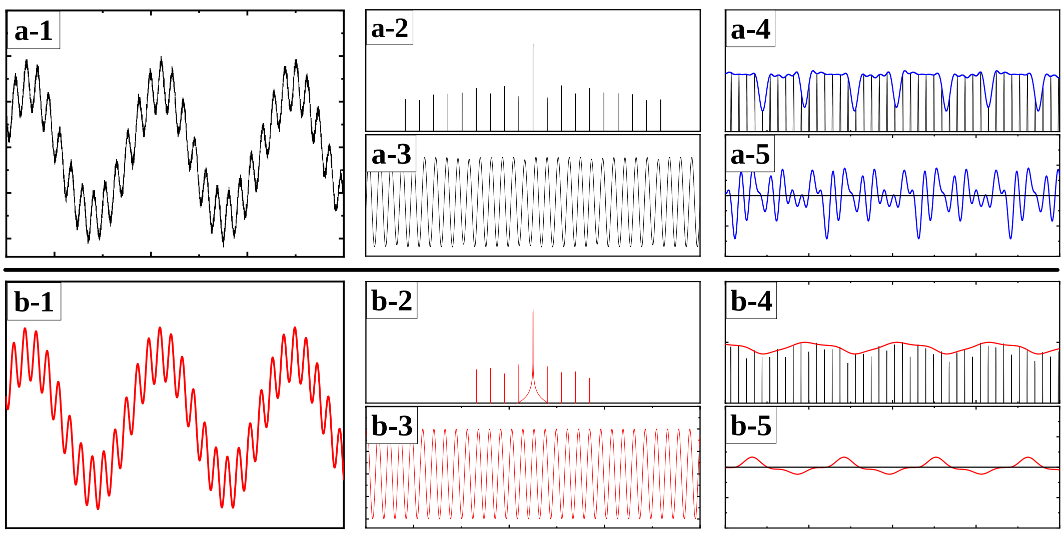

Figure 12 Time-domain transformation procedure results of pre-filtered HT (sampling point 1 of offset 12.5mm): a-1) Experimental signal, a-2, 3) Experimental bandpass-filtered spectrum and signal, a-4, 5) Experimental amplitude and frequency modulation, b-1) Calculated signal, b-2, 3) Calculated bandpass-filtered spectrum and signal, b-4, 5) Calculated amplitude and frequency modulation.

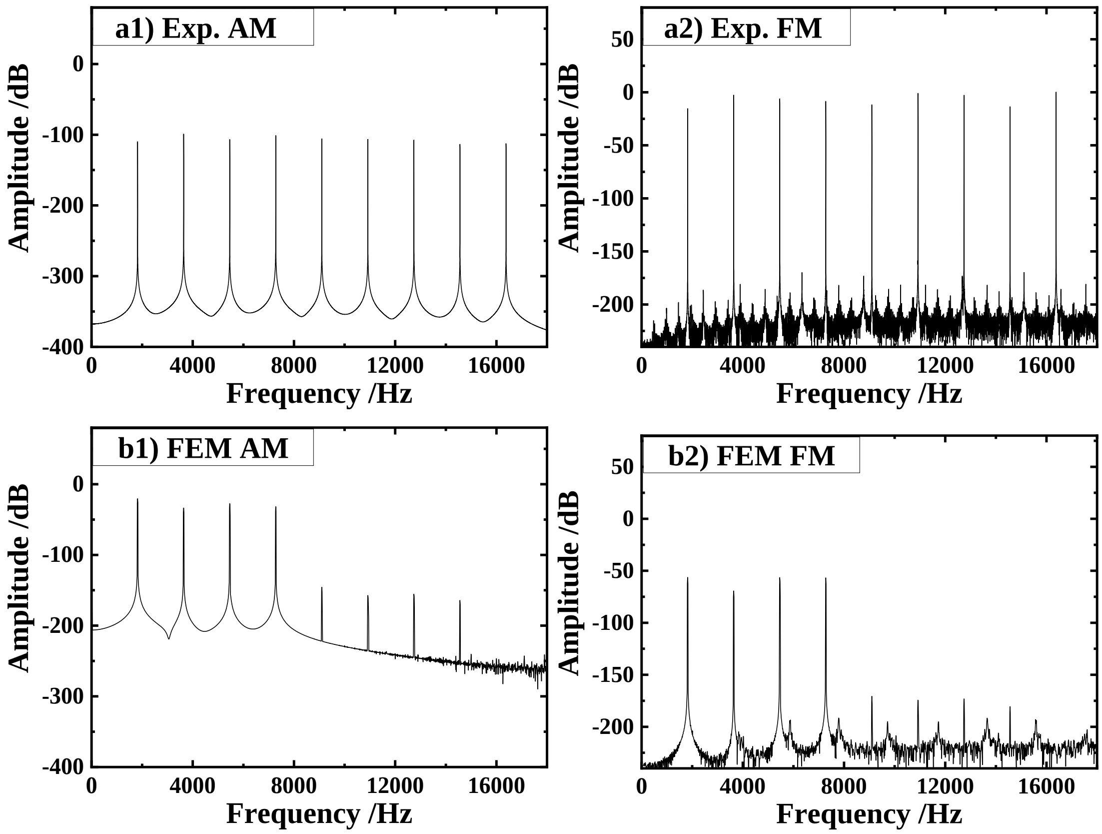

Figure 13 Frequency components of AM and FM (sampling point 1 of offset 12.5 mm).

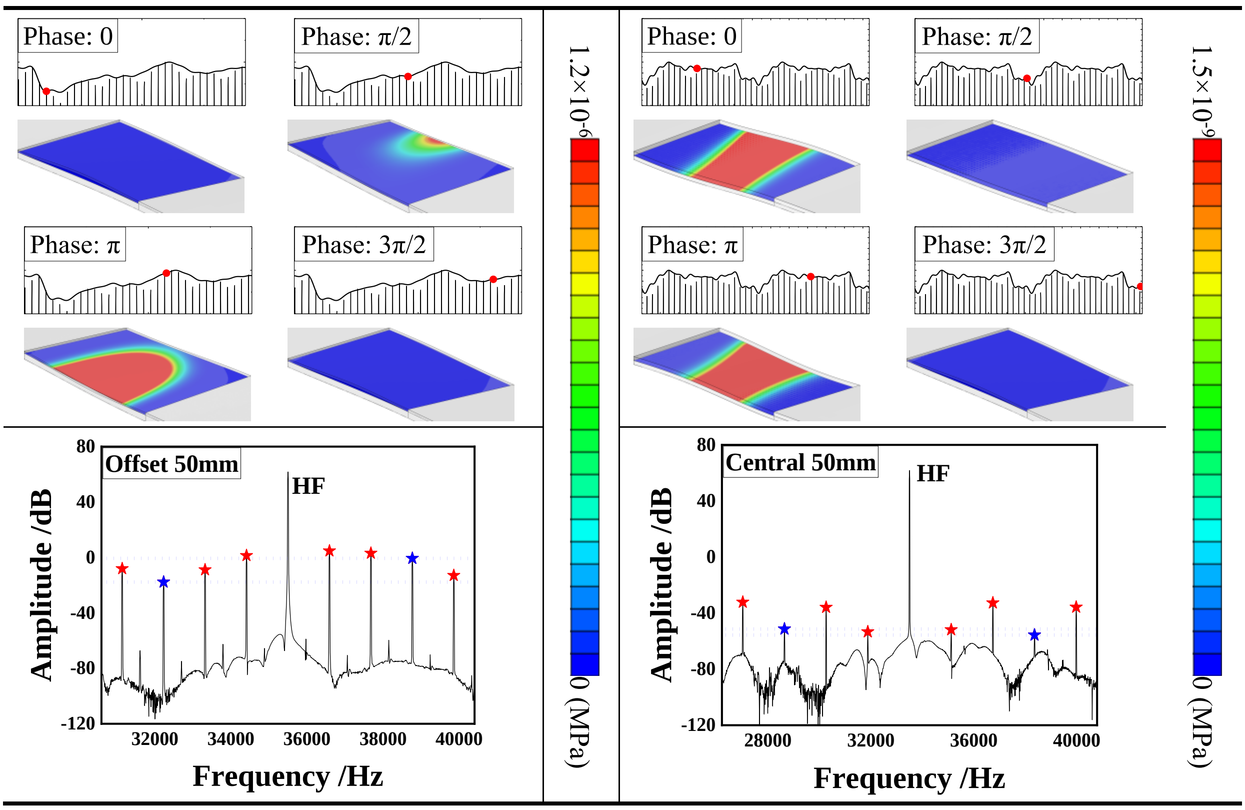

Figure 14 Contact pressure contours at different phases on the offset (Left) and central (Right) 50 mm delamination plates and corresponding spectrums.

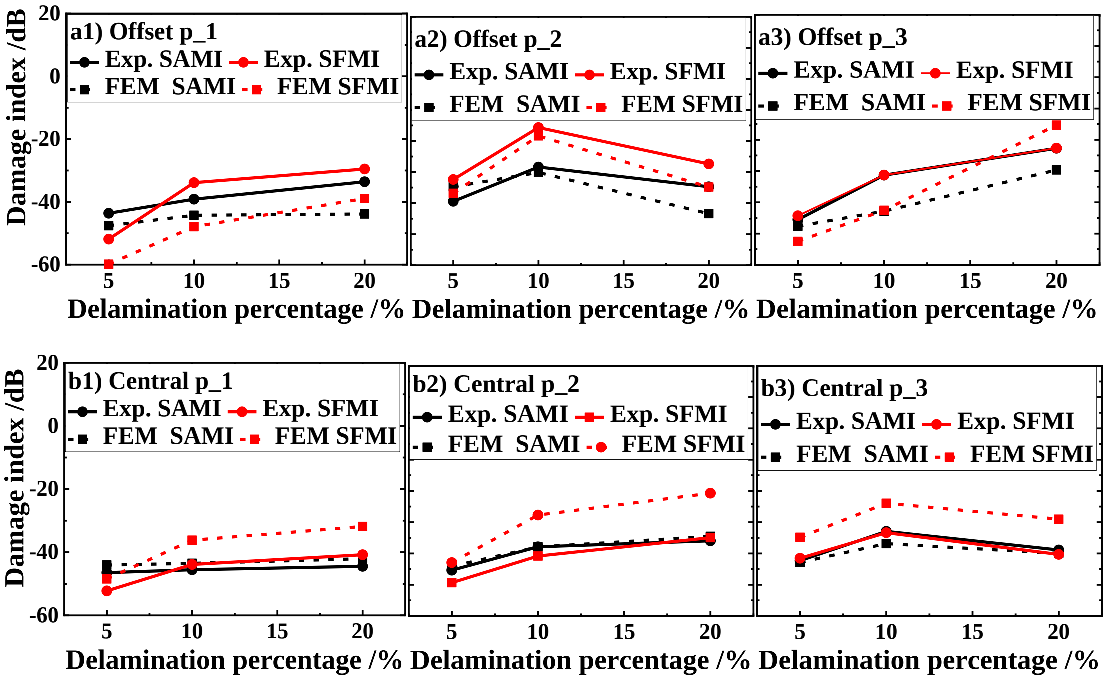

Figure 15 Calculated and experimentally obtained SAMI and SFMI of the 6 delaminated composite plates.

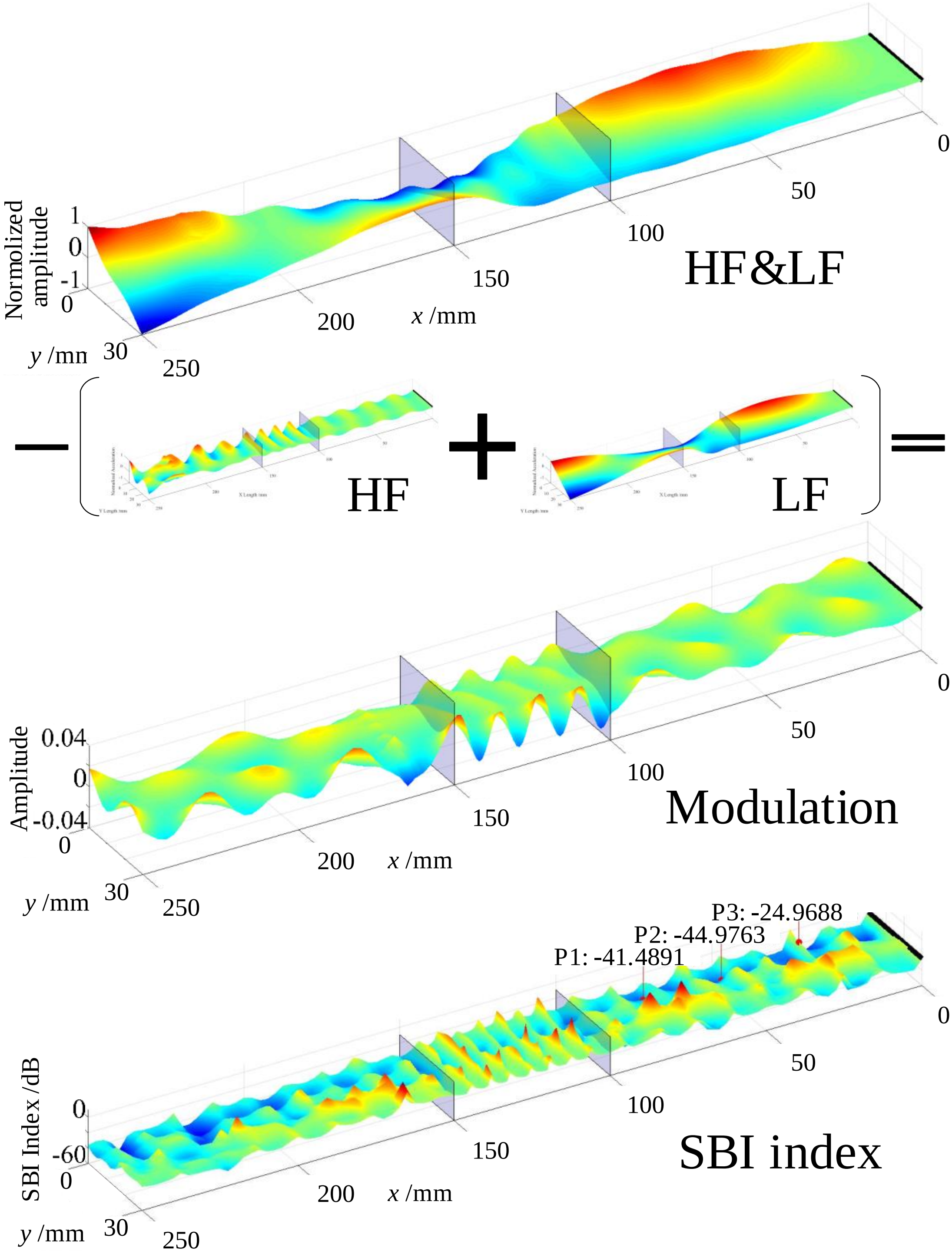

Figure 16 Procedure for extracting the calculated spatial distribution of SBI.

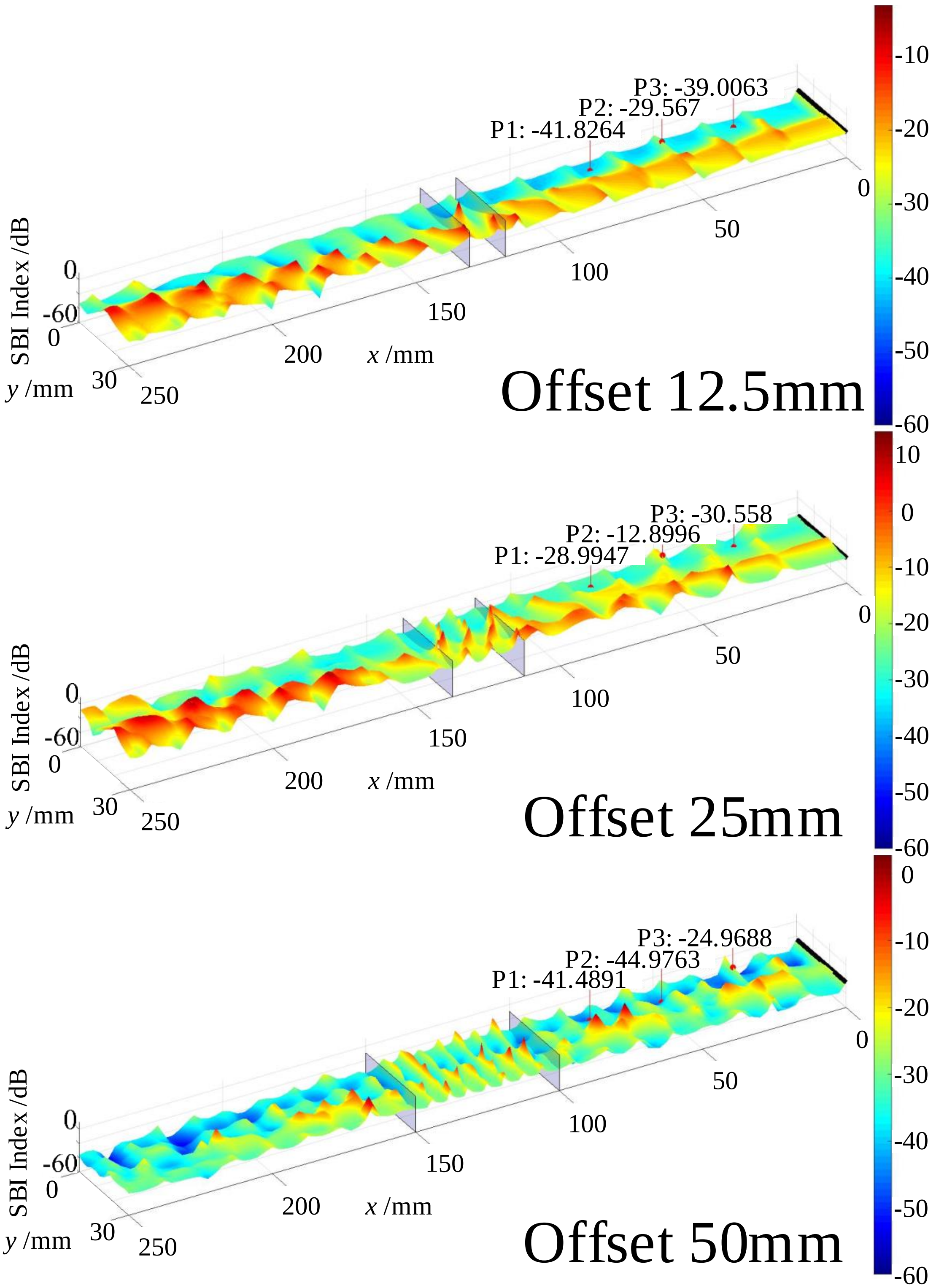
P3: -39.0063
P2: -29.567
P1: -41.8264
SBI Index /dB
0
-60
0
30
y /mm
250
200
150
100
50
0
x /mm
Offset 12.5mm
-10
-20
-30
-40
-50
-60
P3: -30.558
P2: -12.8996
P1: -28.9947
Offset 25mm
10
0
P3: -24.9688
P2: -44.9763
P1: -41.4891
Offset 50mm

1

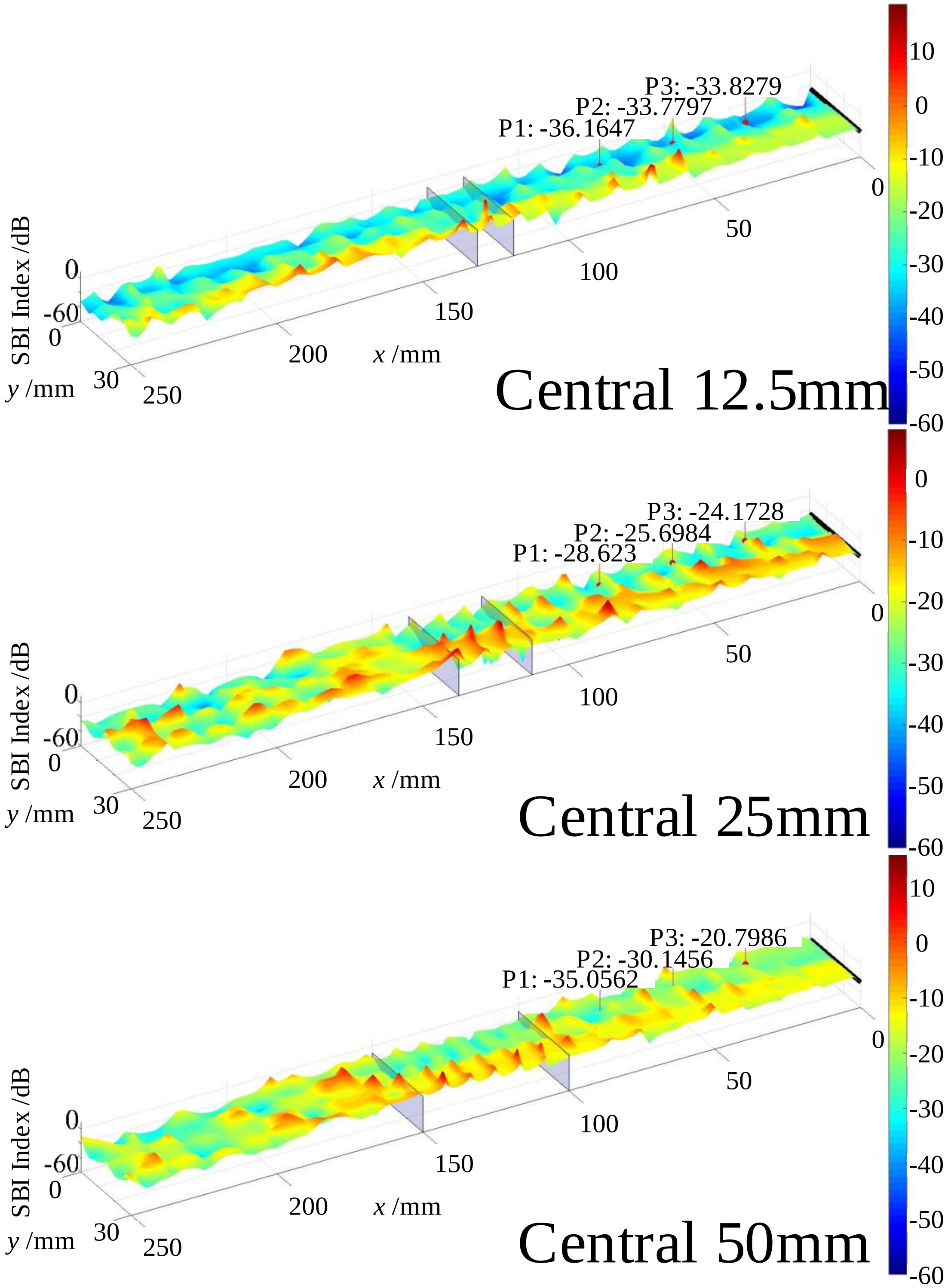

Figure 17 SBI spatial distribution of the 6 delaminated composite plates.

Table 1 Parameters of the modified GW model.

Material properties	Value
E_{f33} (GPa)	15
G_{f23} (GPa)	7.0
β (μm)	6.5
η (mm^{-2})	2.25×10^{6}
r^{*}	6.6×10^{-3}
ψ_N	1.006
ψ_T	0.984
n	5

Table 2 Material properties of the T300/7901 carbon/epoxy composites.

Material properties	Value
E_{11} (GPa)	130.0
E_{22}, E_{33} (GPa)	7.64
G_{12}, G_{13} (GPa)	3.70
G_{23} (GPa)	3.00
υ_{12}, υ_{13}	0.32
υ_{23}	0.45
ρ (g/cm^3)	1.69

Table 3 Selected LFs and HFs.

Specimen		LF (kHz)	HF (kHz)
Offset	12.5mm	1.82	21.45
	25mm	1.79	21.00
	50mm	1.09	35.50
Central	12.5mm	1.77	36.00

25mm	2.20	35.20
50mm	1.62	33.50

Table 4 Peak densities of the delamination and delamination-free areas in all 6 cases

Specimen		Delamination	delamination-free
Offset	12.5mm	0.80cm^{-1}	0.59cm^{-1}
	25mm	1.20cm^{-1}	0.53cm^{-1}
	50mm	1.40cm^{-1}	0.80cm^{-1}
Central	12.5mm	0.80cm^{-1}	0.76cm^{-1}
	25mm	1.20cm^{-1}	0.80cm^{-1}
	50mm	1.00cm^{-1}	0.70cm^{-1}